

The Momentum Budget in the Stratosphere, Mesosphere, and Lower Thermosphere. Part I: Contributions of Different Wave Types and In Situ Generation of Rossby Waves

KAORU SATO AND RYOSUKE YASUI

Department of Earth and Planetary Science, The University of Tokyo, Tokyo, Japan

YASUNOBU MIYOSHI

Department of Earth and Planetary Sciences, Kyushu University, Fukuoka, Japan

(Manuscript received 10 November 2017, in final form 29 June 2018)

ABSTRACT


A momentum budget is examined in the stratosphere, mesosphere, and lower thermosphere using simulation data over ~ 11 years from a whole-atmosphere model in terms of the respective contributions of gravity waves (GWs), Rossby waves (RWs), and tides. The GW forcing is dominant in the mesosphere and lower thermosphere (MLT), as indicated in previous studies. However, RWs also cause strong westward forcing, described by Eliassen–Palm flux divergence (EPFD), in all seasons in the MLT and in the winter stratosphere. Despite the relatively coarse model resolution, resolved GWs with large amplitudes appear in the MLT. The EPFD associated with the resolved GWs is eastward (westward) in the summer (winter) hemisphere, similar to the parameterized GW forcing. A pair of positive and negative EPFDs are associated with the RWs and GWs in the MLT. These results suggest that the RWs and resolved GWs are generated in situ in the MLT. Previous studies suggested that a possible mechanism of RW generation in the MLT is the barotropic/baroclinic instability. This study revisits this possibility and examines causes of the instability from a potential vorticity (PV) viewpoint. The instability condition is characterized as the PV maximum at middle latitudes on an isentropic surface. Positive EPFD for RWs is distributed slightly poleward of the PV maximum. Because the EPFD equals the PV flux, this feature indicates that the RW radiation acts to reduce the PV maximum. The PV maximum is climatologically maintained in both the winter and summer mesospheres, which is caused by parameterized GW forcing.

1. Introduction

In the middle atmosphere, atmospheric waves, such as gravity waves (GWs), Rossby waves (RWs), and tides (TWs), which mainly propagate from the lower atmosphere, are dominant and largely affect the momentum budget. The momentum deposition caused by these waves is the driving force of the mean meridional circulation in the middle atmosphere, which maintains a thermal structure that is partly much different from that expected from the radiative balance. Thus, to better understand the dynamics of the middle atmosphere, particularly the mesosphere and lower thermosphere

(MLT), it is important to examine the relative contributions of these waves to the momentum budget. However, only a few studies on the momentum budget in the MLT have been conducted from this point of view (McLandress et al. 2006; Becker 2012).

GWs originating from the troposphere have the largest impact on the momentum budget in the MLT region. GWs originating from the lower atmosphere have significantly large wind and temperature amplitudes in the MLT region, with low atmospheric density, and hence easily break and deposit the momentum into the mean flow. Such GW forcing acts to maintain a weak-zonal-wind layer and drives the summer-to-winter-pole meridional circulation near the mesopause (e.g., Matsuno 1982; Holton 1983; Plumb 2002). Most general circulation models (GCMs) include the GW forcing using parameterization schemes. The GW forcing is negative (positive) in the winter (summer) upper mesosphere, and the magnitude reaches $100\text{--}160 \text{ m s}^{-1} \text{ day}^{-1}$ at $\sim 60^\circ$ in both hemispheres

 Denotes content that is immediately available upon publication as open access.

Corresponding author: Ryosuke Yasui, yasui.ryosuke@eps.s.u-tokyo.ac.jp

depending on the season and the model (Fomichev et al. 2002; Miyoshi et al. 2014; Becker 2012). The GW forcing around the mesopause in the GCMs is consistent with a recent observational estimate ($\sim 120 \text{ m s}^{-1} \text{ day}^{-1}$ at $z = \sim 87 \text{ km}$) in summer obtained using the mesosphere–stratosphere–troposphere/incoherent scatter (MST/IS) radar at Syowa Station in Antarctica (69.0°S , 39.4°E), which is also called the Program of the Antarctic Syowa MST/IS (PANSY) radar (Sato et al. 2014, 2017).

On the other hand, two specific kinds of RWs, which are called quasi-2-day waves (QTDWs) and 4-day waves, are frequently observed in the summer and winter mesosphere, respectively. According to observational studies conducted using different satellites (e.g., Wu et al. 1996; Lieberman 1999; Limpasuvan and Wu 2003; Garcia et al. 2005; Baumgaertner et al. 2008; Ern et al. 2013) and radars (e.g., Salby and Roper 1980; Murphy et al. 2007), and according to model studies (e.g., Gu et al. 2016), the QTDWs have zonal wavenumbers $s = 2$ –4 and propagate westward, and their activity is maximized slightly after the summer solstice. Recently, Pancheva et al. (2016) conducted a comprehensive study on the QTDWs using global analysis data obtained by a data assimilation system called the Navy Operational Global Atmospheric Prediction System–Advanced Level Physics High Altitude (NOGAPS-ALPHA) over 14 months. They showed that the QTDWs are not due to a single type of waves but are composed of several kinds depending on the latitude and season. The 4-day waves were first reported by Venne and Stanford (1979) using the *Nimbus-5* selective chopper radiometer in the winter stratosphere and are characterized as a mixture of components with $s = 1$ –4 and with the same phase velocity (Prata 1984; Lawrence and Randel 1996; Garcia et al. 2005). According to previous modeling studies (McLandress et al. 2006; Watanabe et al. 2009; Yue et al. 2012), both QTDWs and 4-day waves can provide significant wave forcing, reaching a few tens of meters per second per day in the MLT region. The QTDW forcing estimated by the models is consistent with a recent study by Ern et al. (2013), who used data from the High Resolution Dynamics Limb Sounder and the Sounding of the Atmosphere Using Broadband Emission Radiometry (SABER) satellite instruments. In addition, Ern et al. (2013) indicated large interannual variability of the QTDWs. However, these model studies were based on simulations covering a few to several years. Thus, climatological features of the wave forcing should be examined using data covering as long a period as possible.

One of the most likely excitation mechanisms of these RWs is the barotropic (BT)/baroclinic (BC) instability (e.g., Salby and Callaghan 2001; Manney and Randel 1993). Plumb (1983) examined the BC instability around the strato-mesospheric westward wind and indicated

that the most unstable mode has a zonal wavenumber $s = 3$, which is consistent with observations. In addition, the result obtained via model studies (McLandress et al. 2006; Watanabe et al. 2009) that positive Eliassen–Palm (EP) flux divergence associated with these RWs is observed in the region of negative latitudinal PV gradient is consistent with the RW radiation by the BT/BC instability. A few mechanisms causing the necessary condition of BT/BC instability were proposed by previous studies. Strong RW breaking, such as that which induces the sudden stratospheric warming in winter, significantly reduces the latitudinal gradient of the PV (Baldwin and Holton 1988; Greer et al. 2013). Forcing by gravity waves propagating from the lower atmosphere is another strong candidate (Watanabe et al. 2009; Ern et al. 2013; Norton and Thuburn 1999; McLandress et al. 2006). Most previous studies on forcing discussed the intensification of the mean wind shear due to wave forcing by waves originating from the lower atmosphere. However, consideration of PV yields a more comprehensive and direct interpretation of the BT/BC instability condition formed by these waves. Sato and Nomoto (2015) showed, based on a case study of the Northern Hemisphere (NH) in winter and utilizing a gravity wave resolving general circulation model, that the BT/BC instability condition is characterized as a PV maximum at midlatitudes. This maximum is attributable to an increase in the static stability (or Brunt–Väisälä frequency squared) N^2 due to the upwelling caused by GW forcing.

Tides are dominant at the low and middle latitudes of the MLT region. Large amplitudes of zonal wind components of diurnal westward-migrating tides with $s = 1$ (DW1) are confined to low latitudes below a height of $z = 100 \text{ km}$, while those of semidiurnal westward-migrating tides with $s = 2$ (SW2) extend to high latitudes (Miyahara et al. 1999; Wu et al. 2006). Zhu et al. (2008) showed, using SABER observation data, that the Eliassen–Palm flux divergence (EPFD) associated with DW1 is negative ($\sim -5 \text{ m s}^{-1} \text{ day}^{-1}$) at low latitudes and is positive (10 – $20 \text{ m s}^{-1} \text{ day}^{-1}$) at middle latitudes at $z = \sim 95 \text{ km}$.

Although the RW, GW, and TW are distinguished by their physical properties, their forcings may not be independent. Cohen et al. (2013) showed that excess parameterized GW forcing can be compensated for by the BT/BC instability. This means that accurate observational constraints on GW parameterizations and/or confirmation of resolved waves by observations are important for examining the momentum budget. Because the expression of GWs by current parameterizations is not adequate (e.g., Geller et al. 2013), future projections of the relative contributions of GWs and RWs to the Brewer–Dobson circulation will not be easy

(e.g., Butchart 2014). However, the compensation may truly occur in the real atmosphere.

A method for tackling the dynamics of the compensation mechanism is the utilization of a GW-resolving high-resolution GCM without GW parameterizations. Sato and Nomoto (2015) used such a GCM, called the KANTO model (Watanabe et al. 2008), and elucidated an interesting compensation via a case study of the NH in winter, which is regarded as an interplay of the GWs and RWs. The event starts with a strong RW intrusion from the troposphere to the stratosphere. The RWs break in the upper stratosphere and cause strong wave forcing, which shifts the strato-mesospheric eastward jet poleward. The region of strong GW forcing above the jet also shifts poleward following the jet shift. The GW forcing drives upwelling at the middle latitudes and causes an increase in N^2 . This results in the PV maximum at the middle latitudes satisfying the necessary condition of BT/BC instability. New RWs are radiated to weaken the PV maximum. Such interplay of the GWs and RWs must be present in the real atmosphere; hence, its role in the climatological momentum budget of the middle atmosphere is an interesting topic.

The present study will examine the relative contributions of RWs, GWs, and TWs to the momentum budget in the middle atmosphere, particularly focusing on the MLT region, using simulation data from a whole-atmosphere model [i.e., the Ground-to-Topside Model of Atmosphere and Ionosphere for Aeronomy (GAIA); e.g., Jin et al. (2011)]. Surprisingly and interestingly, resolved GWs appear in the MLT region of the model in spite of the relatively low horizontal resolution. Thus, both resolved and parameterized forcings are examined as the GW contribution. It is also shown that in situ generation of RWs due to the BT/BC instability is a significant factor of the momentum budget. A plausible mechanism of the instability formation in the mesosphere is discussed based on a PV analysis. Satellite observation data from the *Aura* Microwave Limb Sounder (MLS) are also analyzed for validation of the model data. The generation of GWs in the MLT region and its cause will be shown in more detail and discussed in a companion paper (Yasui et al. 2018, hereafter Part II).

The remainder of this paper is organized as follows. A brief description of the data from GAIA and the *Aura* MLS used in this study is given in section 2. The method of analysis is described in section 3. Section 4 shows the climatology of the momentum budget in the middle atmosphere. The characteristics of RWs generated in situ in the mesosphere are examined in section 5. Section 6 discusses the formation of the BT/BC instability in the mesosphere and its relation to the parameterized GW forcing. A summary and the concluding remarks are given in section 7.

2. Data description

Two kinds of data are used for the analysis of the dynamics in the middle atmosphere, particularly in the MLT region. One is simulation data from GAIA, and the other is observation data from the *Aura* MLS (Waters et al. 2006). The time period analyzed in this study is approximately 11 years, from 8 August 2004 to 19 June 2015. The quantitative analysis regarding the momentum budget is performed using mainly the model data. The model results are validated using the observation data as much as possible.

a. GAIA

GAIA is a whole-atmosphere model that covers an altitude range from the surface to the thermosphere/ionosphere. This model is composed of three submodels, namely, a GCM, an ionospheric model, and an electro-dynamical model, which communicate via a coupler module. Only outputs from the GCM component (e.g., Miyoshi and Fujiwara 2003) are used in this study. The model resolution is T42L150, corresponding to a horizontal resolution of $\sim 2.8^\circ$ and vertical grid intervals of 0.2 scale height from the surface (997.5 hPa) to $z = \sim 600$ km (1.017×10^{-9} hPa). The model is nudged toward the JRA-25/JMA Climate Data Assimilation System (JCDAS) data (Onogi et al. 2007) for the altitude range from the surface to ~ 30 km (12 hPa) in order to realistically simulate the quasi-biennial oscillation (QBO) in the equatorial stratosphere and planetary waves originating from the troposphere. Daily values of the 10.7-cm solar radio flux (F10.7) index are included as a proxy of the solar UV–EUV variation. Parameterization schemes for orographic GWs developed by McFarlane (1987) and for nonorographic GWs developed by Lindzen (1981) are implemented as shown in Garcia et al. (2007). The nonorographic GWs are launched at the ~ 200 -hPa level and wave phase speeds of launched GWs are -30 to $+30$ m s^{-1} at an interval of 10 m s^{-1} . The source stress spectrum is specified as a Gaussian, where $\tau_b^* = 6.4 \times 10^{-4}$ Pa for (A21) of Garcia et al. (2007). The resultant latitudinal distribution and magnitude of these parameterized GWs are similar to those described in Geller et al. (2013) at $z = 50$ km. The vertical diffusion coefficient is given according to the Richardson number for each time and grid point (Wu et al. 1989).

An analysis is carried out for an altitude range from the surface to an altitude of $z = \sim 113$ km (1.0×10^{-4} hPa). The time interval of the model output is 1 h. The data used are the zonal wind u , meridional wind v , vertical wind w , temperature T , and geopotential height (GPH). The GW forcing expressed by the

parameterizations is calculated offline using these quantities because it was not archived.

b. Aura MLS

Daily mean temperature T and GPH from the Earth Observation System *Aura* MLS version 3.3/3.4 level 2 (Waters et al. 2006) are used for the analysis. The height range is from 9.4 km (261 hPa) to 97 km (1×10^{-3} hPa). The horizontal and vertical resolutions of the data depend on the height (e.g., 170 km and 5 km at $z = 9.4$ km, and 220 km and 10–13 km at $z = 97$ km, respectively). To make the analysis easier, the original data are averaged for every 24° longitude \times 5° latitude. Note that the *Aura* MLS temperature has a cold bias of ~ 1 K in the troposphere and stratosphere and of ~ 10 K around the mesopause (Schwartz et al. 2008; Medvedeva et al. 2014). Horizontal winds u and v are obtained from the GPH data, assuming gradient wind balance (e.g., Randel 1987; Iida et al. 2014):

$$\begin{aligned} -fv - \frac{uv}{a} \tan\phi &= -\frac{1}{a \cos\phi} \frac{\partial\Phi}{\partial\lambda} \\ fu + \frac{u^2 \tan\phi}{a} &= -\frac{1}{a} \frac{\partial\Phi}{\partial\phi}, \end{aligned} \quad (1)$$

where ϕ , $f(=2\Omega \sin\phi)$, a , Ω , and Φ are the latitude, Coriolis parameter, radius of Earth, angular velocity of Earth's rotation, and geopotential, respectively. The solution closest to the geostrophic wind out of the two solutions of u for the second equation of (1) is used. The gradient wind balance assumption is validated by comparing horizontal wind estimates from the model GPH using (1) with the direct model outputs. The differences are quite small (less than 10%) in the middle atmosphere below $z \sim 90$ km, except for the equatorial region, where the Coriolis parameter is close to zero. In contrast, the differences are more than 30% above $z = 90$ km, where the GW forcing takes a significant role in the momentum balance.

3. Methods of analysis

a. Analysis of wave activity flux and wave forcing

The EP flux and its divergence, which correspond to wave activity flux and wave forcing, respectively, are examined using the transformed-Eulerian-mean (TEM) equation system in the log pressure coordinates. The zonal momentum equation is described as follows:

$$\begin{aligned} \bar{u}_t + \bar{v}^* \left[\frac{1}{a \cos\phi} (\bar{u} \cos\phi)_\phi - f \right] + \bar{w}^* \bar{u}_z \\ = \frac{1}{\rho_0 a \cos\phi} \nabla \cdot \mathbf{F} + \bar{X}, \end{aligned} \quad (2)$$

where overbars ($\bar{}$) and primes (') denote the zonal mean and anomaly from the zonal mean, respectively. In addition, \bar{v}^* and \bar{w}^* are the meridional and vertical components of the residual mean flow, respectively:

$$\bar{v}^* = \bar{v} + \frac{1}{\rho_0} \left(\rho_0 \frac{\bar{v}'\theta'}{\bar{\theta}_z} \right)_z \quad \text{and} \quad (3)$$

$$\bar{w}^* = \bar{w} + \frac{1}{a \cos\phi} \left(\cos\phi \frac{\bar{v}'\theta'}{\bar{\theta}_z} \right)_\phi. \quad (4)$$

The EP flux is

$$\begin{aligned} \mathbf{F} = (0, F^{(\phi)}, F^{(z)}) = \rho_0 a \cos\phi \left\{ 0, \bar{u}_z \frac{\bar{v}'\theta'}{\bar{\theta}_z} - \bar{v}'\bar{u}', \right. \\ \left. \times \left[f - \frac{1}{a \cos\phi} (\bar{u} \cos\phi)_\phi \right] \frac{\bar{v}'\theta'}{\bar{\theta}_z} - \bar{w}'\bar{u}' \right\}, \end{aligned} \quad (5)$$

$$\nabla \cdot \mathbf{F} = \frac{1}{a \cos\phi} \frac{\partial}{\partial\phi} (F^{(\phi)} \cos\phi) + \frac{\partial F^{(z)}}{\partial z}, \quad (6)$$

and \bar{X} is the subgrid-scale nonconservative term, most of which is parameterized GW forcing. As shown in (2), the wave forcing with respect to the zonal mean angular momentum is composed of the EPFD associated with resolved waves and the parameterized GW forcing in the model.

b. Classification of RWs, GWs, and TWs

As mentioned in section 1, resolved GWs with significant amplitudes appear in the model in spite of its coarse horizontal resolution. Thus, the EPFD associated with the resolved GWs and the parameterized GW forcing are examined (separately) as the GW contribution to the momentum budget. The definitions of the RWs, resolved GWs, and TWs in the present study are as follows. First, migrating tides with zonal wave-numbers $s = 1, 2$, and 3 are extracted from the original data as TWs. Second, the remaining components are divided into two categories according to the wave periods: components with periods longer than 24 h are classified as RWs, and those with periods shorter than or equal to 24 h are classified as resolved GWs. The total wave forcing is the sum of the EPFDs caused by the three kinds of resolved waves and the parameterized GW forcing. Note that in our analysis nonmigrating tides are included in the resolved GWs. This is because a significant part of the nonmigrating tides is regarded as inertia GWs having planetary scales (Sakazaki et al. 2015). Thus, we considered that it is better to classify the

resolved waves into RWs and GWs not by the wave-number but by the wave period. Note that the inertial period equatorward of the 30° latitude is longer than 24 h. The results of the RWs in the low-latitude region may be partly reflected by characteristics of the resolved GWs.

c. Potential vorticity analysis regarding barotropic and/or baroclinic instability

The BT/BC instability is one of the plausible mechanisms of the in situ generation of RWs in the mesosphere, although RWs are also directly radiated from the body force caused by GW dissipation and/or breaking (e.g., Holton 1984; Smith 2003). The present study uses the modified potential vorticity (MPV) proposed by Lait (1994), which is defined as Ertel's PV weighted by $\theta^{-9/2}$, for detailed analysis of the BT/BC instability, following Sato and Nomoto (2015):

$$\begin{aligned} \text{MPV} &\equiv P \times \left(\frac{\theta}{\theta_0} \right)^{-9/2} = -g \frac{f + \zeta}{\frac{\partial p}{\partial \theta} \left(\frac{\theta}{\theta_0} \right)^{9/2}} \\ &= \frac{H\theta}{p} \left(\frac{\theta}{\theta_0} \right)^{-9/2} (f + \zeta) N^2 \propto (f + \zeta) N^2, \end{aligned} \quad (7)$$

where P , θ , θ_0 , g , ζ , N^2 , and p denote Ertel's PV, the potential temperature, the reference potential temperature, the gravitational acceleration, the relative vorticity, the Brunt–Väisälä frequency squared, and pressure, respectively. The necessary condition of BT/BC instability is described using the zonal-mean MPV ($\overline{\text{MPV}}$),

$$\left. \frac{\partial \overline{\text{MPV}}}{\partial \phi} \right|_{\theta} < 0, \quad (8)$$

somewhere. As MPV values do not largely depend on θ , it is easy to examine the vertical structure of the latitudinal distribution of the PV. In addition, as seen from (4), the MPV is proportional to the absolute vorticity $f + \zeta$ and to N^2 . This means that an anomalous PV structure, if it appears, is due to the relative vorticity and/or due to N^2 with significant intensity.

4. Comparison of the mean and wave fields between the model and observation

Figure 1 shows latitude–height sections of the climatology of \bar{T} and \bar{u} during January made using *Aura* MLS observation and GAIA simulation data covering a

period of 11 years. The overall features in the observation and model fields are quantitatively similar. The summer westward jet in the middle atmosphere tilts poleward with height, while the winter eastward jet tilts equatorward with height. Such wind characteristics are related to the latitudinal structure in \bar{T} by the thermal wind balance. The difference in \bar{T} between the model simulation and observations is large in the MLT region. One of the likely reasons is the aforementioned cold bias of the *Aura* MLS observations. Another likely reason is weaker meridional circulation driven by GWs in the model. This influence is consistent with warmer (colder) temperatures in the summer (winter) mesopause region in the model than in the observations. A notable difference between the model and observation is also seen in the wind field. A wind reversal in the vertical direction for the summer upper mesosphere is located at ~ 95 km in the *Aura* MLS observations while it is obscured in the model. This feature is consistent with the temperature difference and hence also attributable to weaker GW forcing. However, it should be noted that a significant eastward vertical gradient above the westward jet (near 90 km) is well simulated by the model. The other notable difference in \bar{u} is observed at low latitudes above 50 km, particularly for the winter hemisphere. The difference is mainly due to the dominance of tides in this region (i.e., MLS observations are sun synchronous at 1345 LT ascending equator-crossing time) and partly due to the departure from the gradient wind balance at the low latitudes with a small value of f . In the present study, further analysis is focused on the region below $z = 100$ km.

Figures 1c and 1f show the EP flux and EPFD for January from *Aura* MLS and GAIA, respectively. Because the *Aura* MLS data do not include the w component, the term proportional to $\overline{w'u'}$ in (9) is ignored for the EP flux calculation. Thus, the EP flux and EPFD in Fig. 1 are mainly due to the RWs. Overall, for the RWs, the features in the observations and model simulation are also quantitatively similar. Strong upward and slightly equatorward EP fluxes originating from the troposphere are observed in the winter stratosphere in the NH. The divergence of the upward EP fluxes is strongly negative at middle latitudes around $z = 50$ km. An interesting feature is the existence of strong upward and slightly equatorward EP fluxes in the summer MLT region. The EP fluxes in the summer MLT region in the Southern Hemisphere (SH) are considered to be not due to RWs propagating from the troposphere but due to in situ generated RWs in the mesosphere because of the following two reasons. First, stationary RWs originating from the troposphere cannot propagate into the westward wind in the summer stratosphere

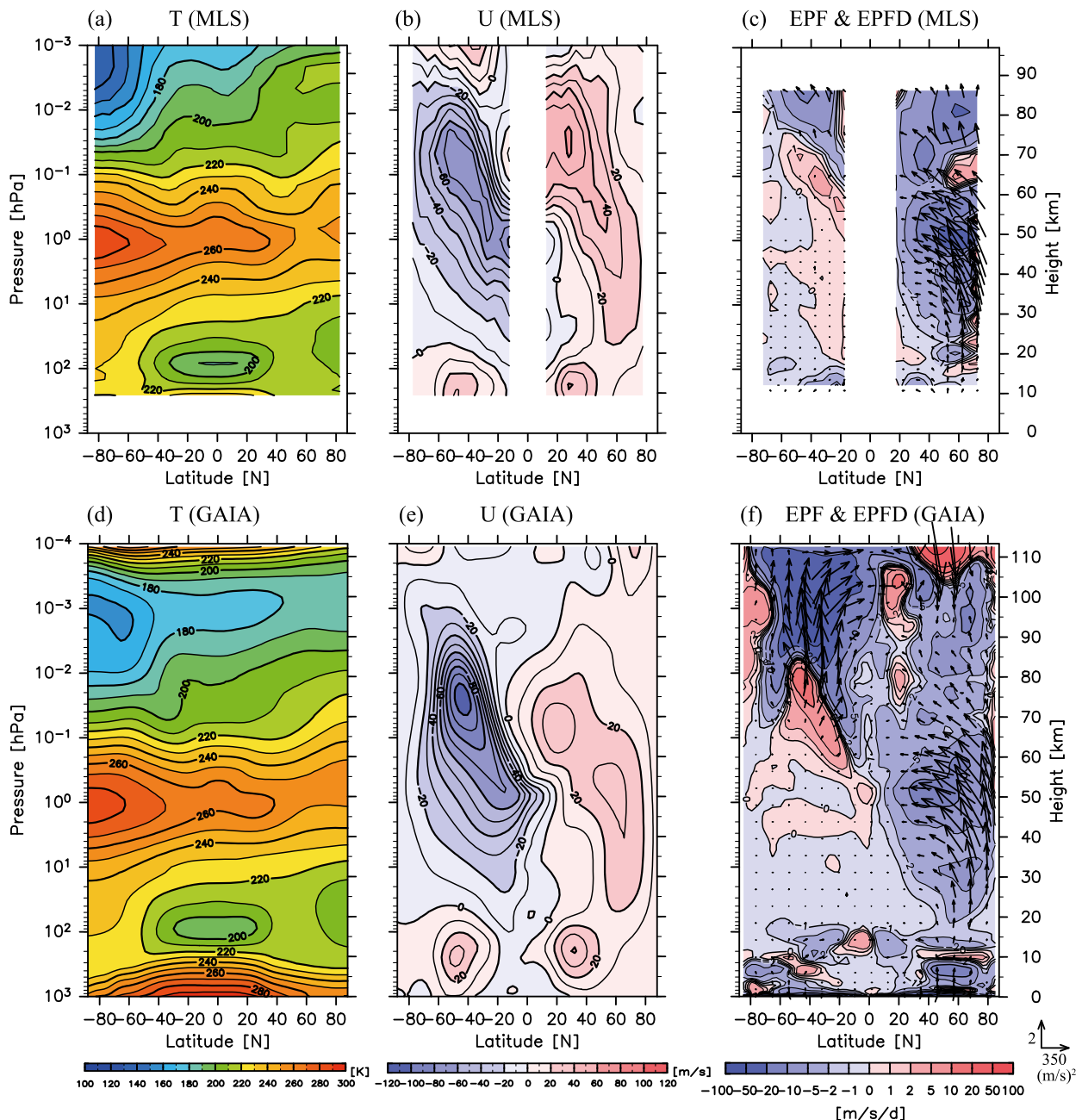


FIG. 1. Latitude–height sections of January climatology of the (left) zonal-mean temperature, (center) zonal wind, and (right) EP flux, ignoring a term proportional to $u'w'$ (arrows) and its divergence (color shading). Results from the (a)–(c) *Aura* MLS observation and (d)–(f) GAIA model. Contour intervals of the temperature and zonal wind are 10 K and 10 m s^{-1} , respectively. Note that the contour intervals of the EP flux divergence are not uniform.

(Charney and Drazin 1961). Second, positive EPFD is observed at higher latitudes near the bottom of the strong upward EP flux. A similar feature is also seen in the EP flux of QTDWs of SABER observations (Ern et al. 2013). The T amplitude of QTDWs with $s = 3$, which is dominant in the summer mesosphere, is $\sim 8 \text{ K}$ at $\phi = 40^\circ \text{S}$ and $z = 80 \text{ km}$ during January 2006 in GAIA. This result

is also consistent with that of the SABER observations shown by Ern et al. (2013). Upward and equatorward EP fluxes are also observed in the winter MLT region, although they are slightly weaker than those in the summer MLT region, particularly in the *Aura* MLS data. The EP fluxes in the winter MLT region may also be due to in situ generated RWs in the mesosphere because the

EPFD is positive at high latitudes near $z = 70$ km, although this is not very clear from the GAIA data.

It should be also noted that TWs simulated by GAIA are also realistic. The maximum amplitudes of temperature, zonal wind, and meridional wind for diurnal migrating tides are ~ 7 K, $\sim 15 \text{ m s}^{-1}$, and $\sim 20 \text{ m s}^{-1}$ at $z = \sim 100$ km, respectively (see Fig. 7 in Part II). These are in good agreement with the amplitudes observed by SABER (Zhu et al. 2008; Mukhtarov et al. 2009). In contrast, the maximum amplitudes of semidiurnal migrating tides are ~ 8 K for T , $\sim 30 \text{ m s}^{-1}$ for u , $\sim 30 \text{ m s}^{-1}$ for v at $z \sim 105$ km in GAIA. These amplitudes are $\sim 20 \text{ m s}^{-1}$ for u and $\sim 20 \text{ m s}^{-1}$ for v larger than the SABER observations in Zhu et al. (2008) at $z = 105$ km.

In summary, roughly speaking, the model fields are consistent with observations for the zonal mean field and RW fields. Thus, further detailed analysis regarding the momentum budget in the middle atmosphere is carried out using model data in the following sections.

5. Momentum budget in the middle atmosphere

a. Total wave forcing

Figure 2 shows the climatology of total wave forcing, which is the sum of the EPFD, including the term $\overline{w'u'}$, and parameterized GW forcing (top panels), together with \overline{T} and \overline{u} (bottom panels), in the latitude–height sections for January, April, July, and October, obtained using the model data. Overall, the characteristics of the total wave forcing are similar between the NH and SH. The total wave forcing is negative (westward) throughout the whole middle atmosphere in autumn and winter, while it is positive (eastward) in the mesosphere in summer. In spring, the total wave forcing is negative below $z \sim 70$ km, while it is positive above $z \sim 70$ km. The direction of total wave forcing is generally opposite that of \overline{u} in each region.

However, there are a few notable differences between the two hemispheres. As is well known, the total wave forcing in the winter stratosphere is stronger in the NH than in the SH, reflecting the difference in wave activity of stationary RWs (usually called planetary waves). In addition, the total wave forcing in spring is stronger in the SH than in the NH. This is due to the longer duration of the polar night jet in the SH, which provides more preferable conditions for RWs to penetrate into the stratosphere.

Here, we note two important correspondences between the wave forcing and zonal wind in the MLT region, which are related to the discussion later in this paper. First, strong positive (eastward) wave forcing in the summer mesosphere is distributed along the low-latitude side of the summer westward jet, tilting

poleward with height. This feature is consistent with the SABER observations, although the analysis by the SABER observations provided only absolute values of the wave forcing (e.g., Ern et al. 2011). This suggests that the strong latitudinal and vertical shear of the westward jet is maintained by the wave forcing. Second, negative wave forcing in the winter hemisphere is maximized at middle and high latitudes around $z = 70$ km. This forcing is seemingly related to the separation of the eastward jet in the middle atmosphere into two jets, namely, the lower (i.e., $z \cong 50$ km) one at high latitudes and the upper (i.e., $z \cong 70$ km) one at low latitudes, which is particularly clear in the NH in January. It is worth noting that another strong forcing region observed in the summer polar region should be neglected because this is due to unrealistically strong sources given in the gravity wave parameterization (Geller et al. 2013), as shown in the following section including potential vorticity analysis in section 6a.

b. Each wave forcing

Figure 3 separately shows the latitude–height sections of the climatology of the EP flux and EPFD associated with RWs, resolved GWs, and TWs and the parameterized GW forcing (GWF_P) for January, April, July, and October. First, the characteristics of each wave contribution will be shown; second, the contribution of each wave to the total wave forcing will be discussed.

The characteristic features of RWs in January were already discussed in section 4. The strong upward and slightly equatorward EP fluxes in the stratosphere in January in the NH for RWs are also observed in July and October in the SH, and they are quite weak in April in the NH. However, there are a few regions with positive EPFD even in the stratosphere, suggesting the presence of nonlinear processes. The divergence of the upward EP fluxes is strongly negative at middle latitudes in the lower mesosphere slightly above $z \sim 50$ km in solstitial seasons. Strong upward EP fluxes in the MLT region associated with positive EPFD at their bottom are observed in July as well as in January. The EPFD in the MLT region is mainly negative. Similar characteristics of the EPFD of RWs were seen in the results of McLandress et al. (2006), although the positive EPFD of RWs in the summer mesosphere was small in their analysis and the EP fluxes were not shown. As already discussed, the EP fluxes observed in the MLT region are likely due to in situ generated RWs in the mesosphere. EP fluxes and the EPFD in the MLT region in equinoctial seasons exhibit a complicated structure, but the EPFD tends to be positive at low latitudes and negative at middle and high latitudes in the autumn hemisphere.

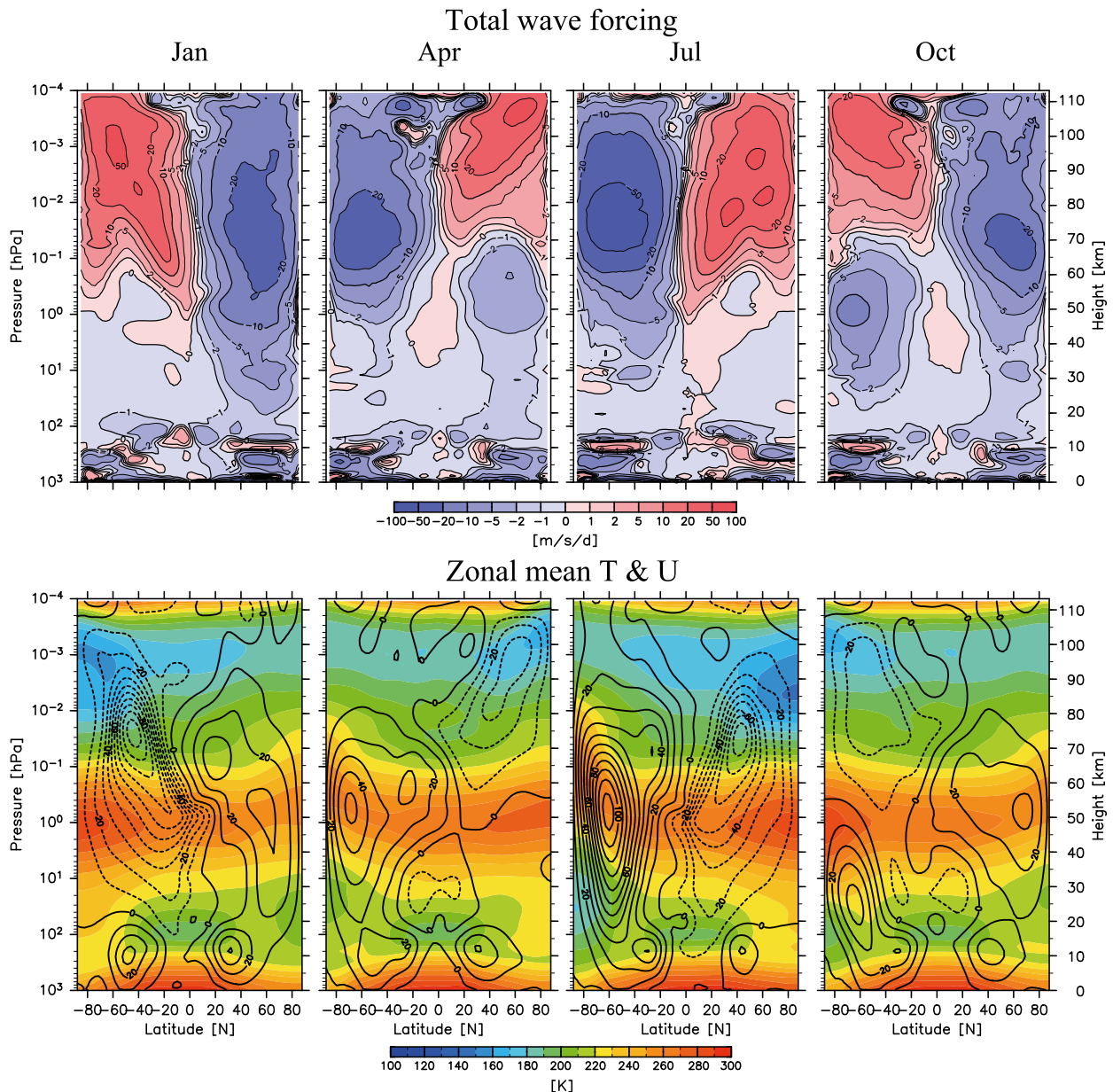


FIG. 2. Latitude–height sections of (top) zonal-mean total wave forcing ($\text{m s}^{-1} \text{day}^{-1}$) and (bottom) zonal-mean temperature (colors) and zonal wind (contours) for climatology in (left to right) January, April, July, and October. Contour intervals of temperature and zonal wind are 10 K and 10 m s^{-1} , respectively. Note that the contour intervals of the total wave forcing are not uniform.

Significant EP fluxes associated with resolved GWs are observed in the MLT region in all seasons. We considered that the components designated “resolved GWs” are GWs because the EP fluxes are mainly due to $\overline{w'u'}$ and exhibit features much different from those associated with RWs. Figure 4 is the same as Fig. 3, but for the EP flux only due to $\overline{w'u'}$ and its divergence for resolved GW components. It is clear that the features in Fig. 4 are quantitatively consistent with those in Fig. 3

for resolved GWs. Note that negative (positive) $\overline{w'u'}$ is expressed by upward (downward) EP flux. The EP fluxes are mainly downward (upward) during the spring and summer (autumn and winter) MLT regions. The EPFD caused by resolved GWs are mainly positive (negative) in the spring and summer (autumn and winter) and maximized around $z = 100 \text{ km}$ in the lower thermosphere. The magnitudes of the positive EPFD in the summer (spring) hemisphere are larger than those

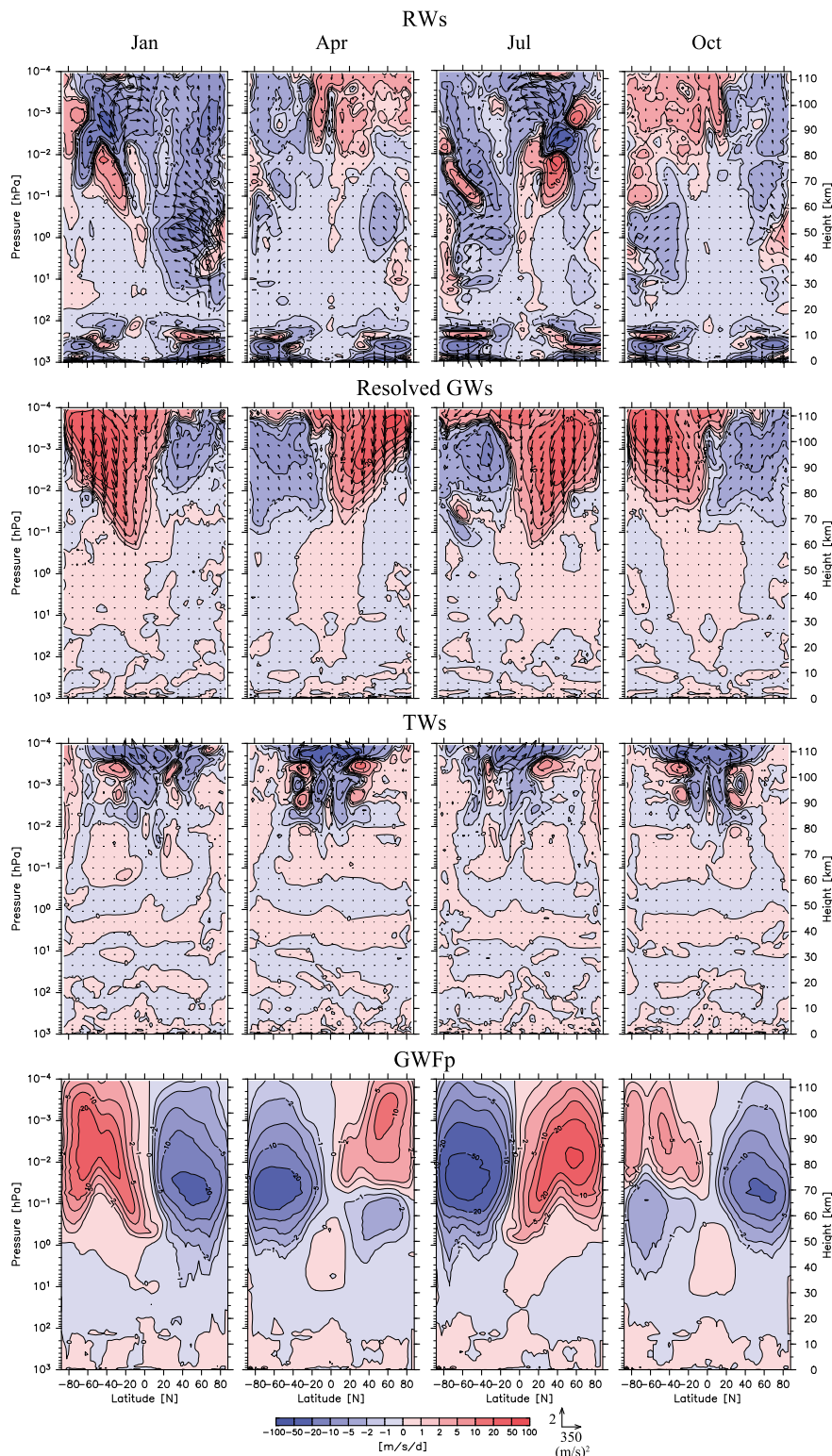


FIG. 3. Latitude–height sections of EP flux and EP flux divergence of the (top to bottom) RWs, resolved GWs and TWs, and parameterized GW forcing for climatology in (left to right) January, April, July, and October. Arrows denote EP flux ($\text{m}^2 \text{s}^{-2}$). Note that the contour intervals are not uniform, but the color contours for the EP flux divergence and parameterized GW forcing are taken to be the same for all panels.

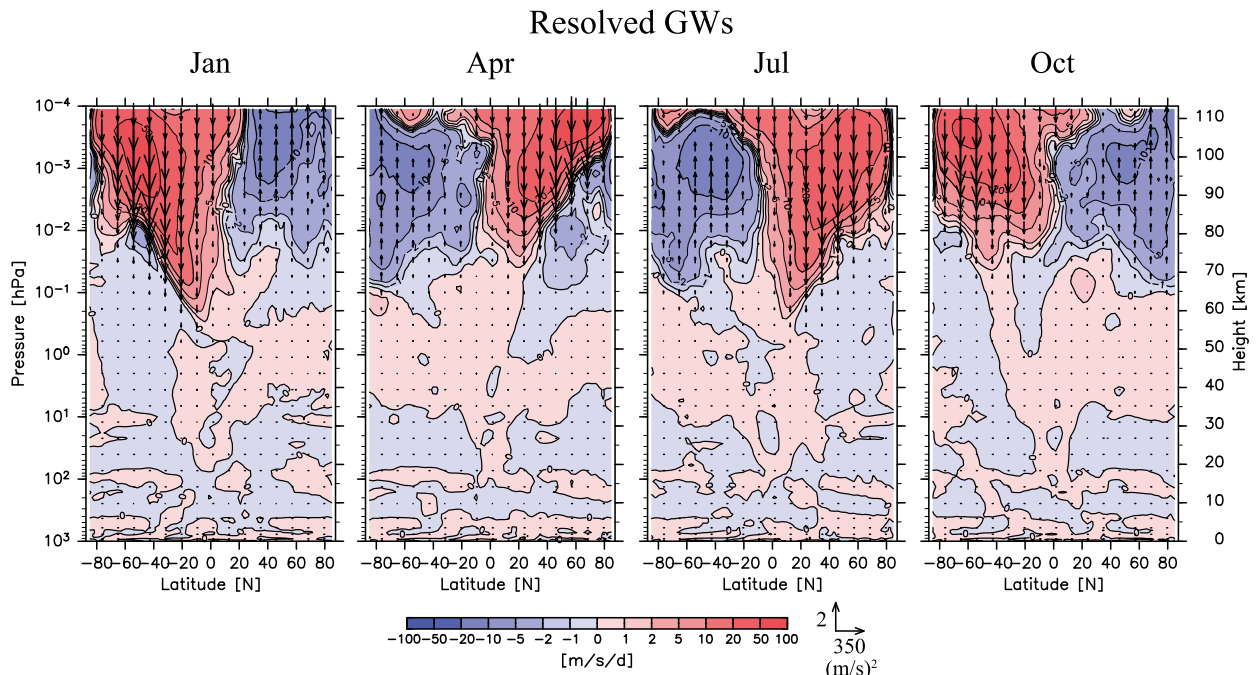


FIG. 4. As in Fig. 3, but for $\rho_0 a \cos \phi \overline{w'u}$ associated with resolved GWs.

of the negative EPFD in the winter (autumn) hemisphere. It will be shown in detail in Part II that the resolved GWs are likely generated in situ in the mesosphere, although some of the resolved GWs may originate from the troposphere as nonmigrating tides (e.g., Sakazaki et al. 2015). McLandress et al. (2006) showed the EPFDs of both all resolved waves and $s = 1-4$, and indicated that there were significant differences between them from $z = \sim 80$ to ~ 130 km. It is possible that these differences are attributable to resolved GWs, although the possibility of GWs was not documented in their paper.

The contribution of TWs to the momentum budget is large at low latitudes, particularly in equinoctial seasons. EP fluxes and the EPFD are negative near the equator for $z = 80-100$ km and positive at $\phi = 30^\circ$ for $z = 90-100$ km. These characteristics are consistent with those of DW1 (e.g., Lieberman and Hays 1994). It is also worth noting that upward EP fluxes and negative EPFD are widely seen at low and middle latitudes above $z \sim 100$ km. These are likely a mixture of DW1 and SW2.

GWF_P is mainly positive (negative) in the summer (winter) MLT region, similar to the EPFD caused by resolved GWs. Positive GWF_P in the summer upper mesosphere has two maxima located at low to middle latitudes and at high latitudes. The high-latitude maximum reflects the total wave forcing and should be neglected because it is likely too strong a source of fluxes given in the GW parameterization, as indicated by

(Geller et al. 2013) based on a comparison of parameterized GW forcing with observations and GW-resolving model simulations. In contrast, negative GWF_P in the winter hemisphere has a single maximum at middle latitudes. It is interesting that the maxima of the positive and negative GWF_P in the solstitial seasons are located at lower altitudes than those of EPFD caused by resolved GWs. The features during the equinoctial seasons are interesting. The GWF_P in autumn is negative, and its distribution is similar to that in winter. In contrast, GWF_P in spring is negative below $z = 70$ km and positive above. This is likely related to the appearance of the westward jet in the MLT region. However, the height of the zero contour for GWF_P is slightly different from and lower than that for \bar{u} . This means that GWF_P accelerates the lower part of the westward jet and contributes to the formation of the summer jet.

Next, the contribution of each wave to the total wave forcing is examined by comparing features observed in Figs. 2 and 3. During solstitial seasons, the wave forcing in the MLT region (i.e., $z > 50$ km) is mainly contributed to by resolved and parameterized GWs. The EPFD caused by RWs tends to mitigate the GW forcing in the summer MLT region, except for the positive EPFD observed at middle to high latitudes around $z = 70$ km. In contrast, the EPFD caused by RWs reinforces the GW forcing in the winter MLT region. The EPFD caused by RWs has magnitudes that are comparable to

those caused by resolved GWs for both the summer and winter seasons, indicating that the EPFD due to RWs generated in the mesosphere is not negligible in the MLT region. In the stratosphere, the total wave forcing is large in winter and mostly attributable to the EPFD due to RWs and partly to GWF_P , particularly for the upper stratosphere. The total wave forcing and each wave forcing in the summer stratosphere are small.

Contributions by respective waves in the stratosphere and MLT region in autumn are similar to those in winter, although the magnitude is relatively small. The total wave forcing in spring is mainly negative for $z < 70$ km and positive for $z > 70$ km. This structure is mainly attributable to the GWF_P , but the EPFD due to resolved GWs contributes largely in the upper region, and the contribution of RWs is large in the lower region. It may also be worth noting for equinoctial seasons that the EPFD associated with TWs at low latitudes is largely canceled by that associated with RWs.

In summary, the total wave forcing, as a measure of the momentum budget, is basically determined by RWs in the winter stratosphere and by parameterized GWs in the MLT region. The contribution of parameterized GWs is large in the equinoctial stratosphere. However, RWs and resolved GWs in the MLT region, which are likely generated in situ in the mesosphere, make a significant contribution to the momentum budget. The TW contribution is limited to the low-latitude region of the lower thermosphere. Note that resolved GWs in GAIA may be largely different from GWs in the real atmosphere because of the relatively coarse horizontal resolution of the model. However, considering that the mean fields simulated in GAIA are in good agreement with observations (Figs. 1b,e) and that the features of EP flux and EPFD associated with RWs simulated in GAIA are also realistic (Figs. 1c,f), to simulate the realistic mean fields, it is likely that the EPFD of resolved GWs is realistic in GAIA.

6. Rossby waves generated in the MLT region

As discussed in the last section, some evidence exists suggesting the in situ generation of RWs in the mesosphere. First, RWs generated in the troposphere hardly propagate upward in summer because the stratospheric mean wind is westward. Second, positive EPFD is observed at high latitudes of the mesosphere in both the summer and winter seasons. A likely mechanism of the RW generation in the mesosphere is BT/BC instability. In this section, the instability condition is examined in terms of PV from a climatological viewpoint regarding the robustness, seasonal variability, and maintenance mechanism. Moreover, characteristics of the in situ

generated RWs in the mesosphere and their relation to the anomalous PV structure are studied.

a. Modified potential vorticity in the MLT region

Figure 5 shows the $\overline{\text{MPV}}$ climatology and its latitudinal gradient $\overline{\text{MPV}}_\phi$ in January and July in the meridional cross section, with the vertical axis indicating the potential temperature. Green contours indicate the log-pressure height. Note that the log-pressure height contours are not necessarily horizontal, suggesting that the latitudinal gradient of the PV over the isentropic surface cannot be replaced with that over the isobaric surface to examine the BT/BC instability. The local maxima of $|\overline{\text{MPV}}|$ are observed in the mesosphere of both hemispheres, namely, at $\phi \sim 30^\circ$ in the summer hemisphere and at $\phi \sim 40^\circ$ in the winter hemisphere in the θ region of 3000–5000 K ($z \sim 65$ –85 km). A negative gradient of $\overline{\text{MPV}}$ extending equatorward and downward is present at the high latitude of each $|\overline{\text{MPV}}|$ maximum, satisfying the necessary condition of the BT/BC instability. This fact indicates that the BT/BC instability does not rarely occur but is robust in solstitial seasons. It is interesting that the negative $\overline{\text{MPV}}_\phi$ regions at middle latitudes for $\theta = 3000$ –5000 K correspond to those with positive EPFD due to RWs (see Fig. 3), suggesting that the RWs in the MLT region are generated via the BT/BC instability. Note that another negative $\overline{\text{MPV}}_\phi$ region is observed at high latitudes for $\theta = 7000$ –10 000 K in the southern summer hemisphere. These negative $\overline{\text{MPV}}_\phi$ regions are also simulated in McLandress et al. (2006), but the top of height of negative $\overline{\text{MPV}}_\phi$ regions is lower ($z = \sim 85$ km) than that in McLandress et al. (2006) ($z = \sim 100$ km). This difference may be caused by $\overline{\text{MPV}}_\phi$ calculation in not isentropic coordinates but log-pressure height coordinates in their study. An analysis of this region was not made, however, because this anomalous $\overline{\text{MPV}}_\phi$ is probably caused by the aforementioned unrealistically strong GWF_P .

The characteristic features of the $\overline{\text{MPV}}$ observed in the model simulation are also seen in the *Aura* MLS observations. Figure 6 shows the meridional cross section of the $\overline{\text{MPV}}$ and $\overline{\text{MPV}}_\phi$ climatologies. The values of the $|\overline{\text{MPV}}|$ are maximal at middle latitudes around $z \sim 70$ km, and negative $\overline{\text{MPV}}_\phi$ is observed poleward of the maximum. The regions with negative $\overline{\text{MPV}}_\phi$ agree well with the positive EPFD regions (Fig. 2). These consistencies between the model simulation and satellite observations strongly suggest that RW generation in the mesosphere via the BT/BC instability is robust also in the real atmosphere and that the model data can be used as a surrogate of the real atmosphere data.

Next, seasonal variations of the $\overline{\text{MPV}}$ and EPFD are examined using model data. Figure 7a shows the time–latitude sections of the $\overline{\text{MPV}}$ (contours) and $\overline{\text{MPV}}_\phi$

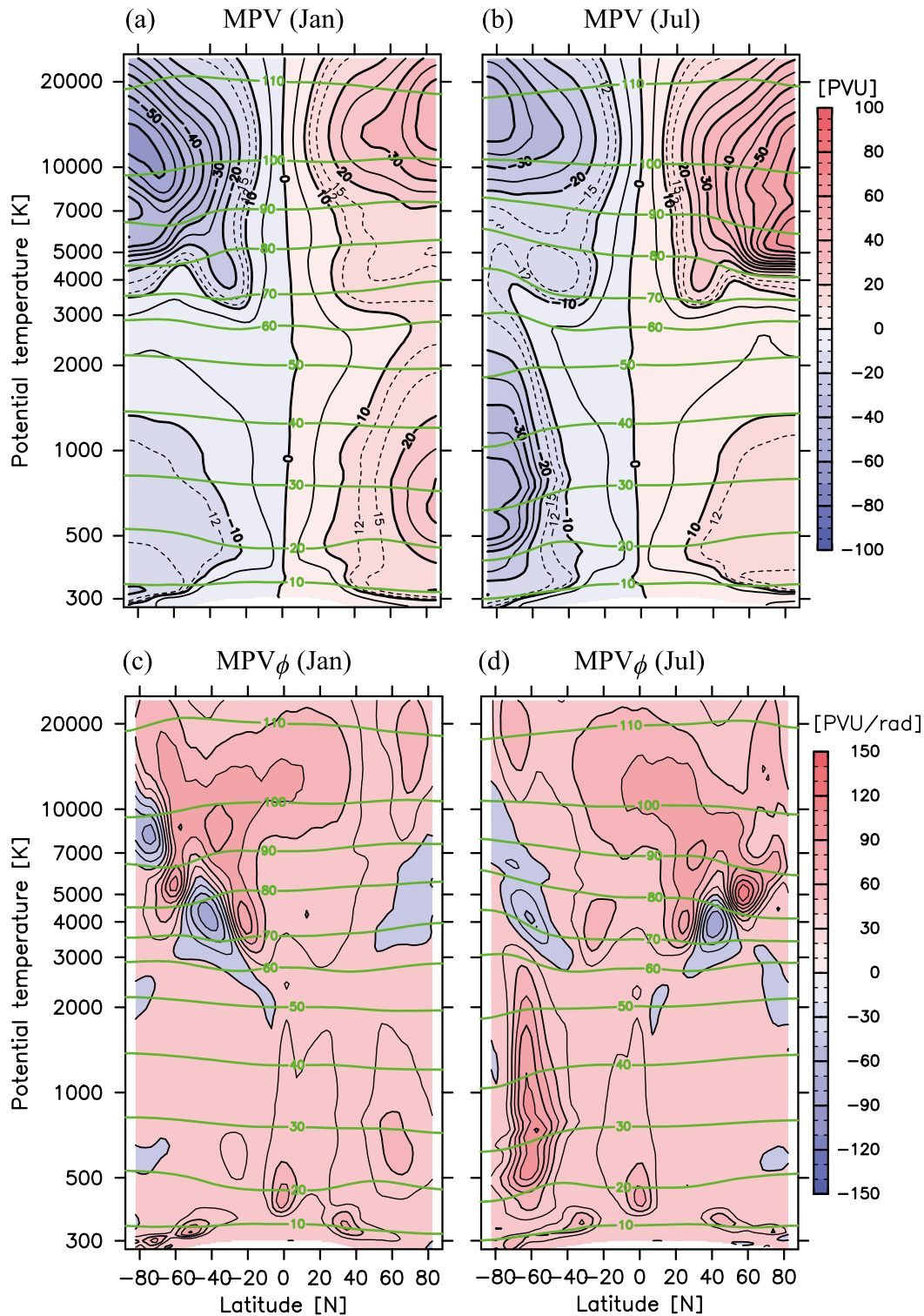


FIG. 5. Meridional cross sections of climatology of (a),(b) \overline{MPV} and (c),(d) \overline{MPV}_ϕ for (left) January and (right) July obtained from the GAIA data. Potential temperature θ is used for the vertical axis. Contour intervals of \overline{MPV} and \overline{MPV}_ϕ are 5 PVU and 15 PVU rad^{-1} , respectively. Green curves show contours of the geopotential height at an interval of 10 km.

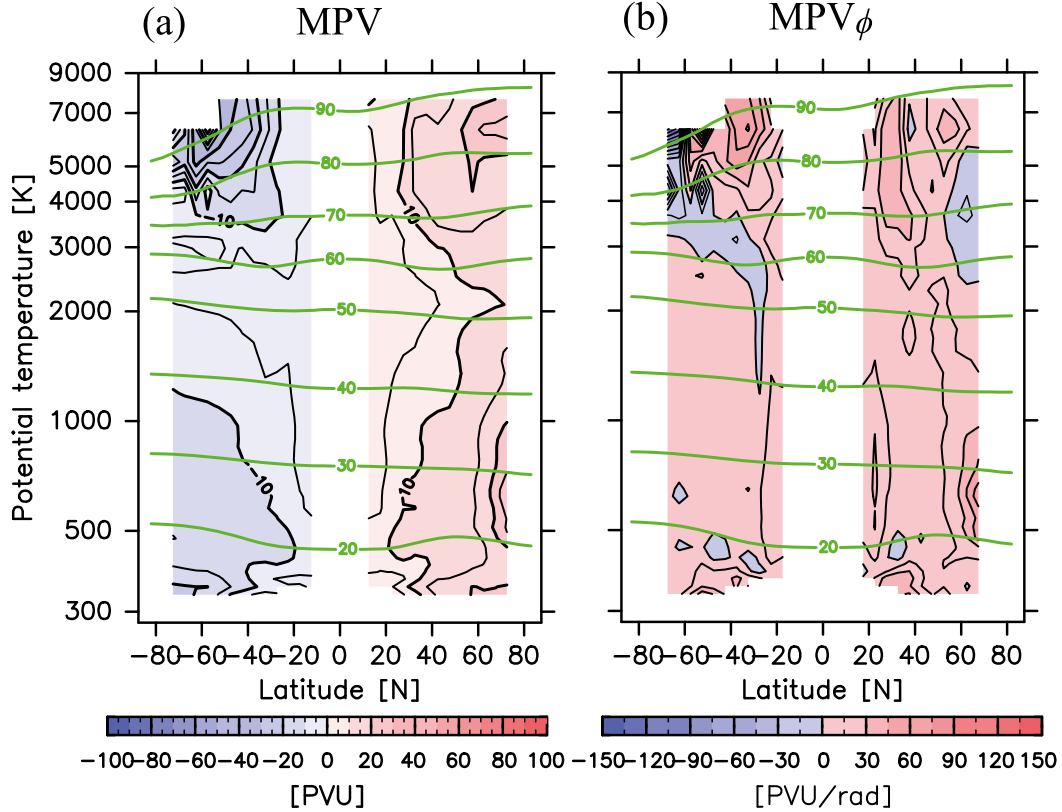


FIG. 6. Meridional cross sections of climatology of (a) \overline{MPV} and (b) \overline{MPV}_ϕ for January obtained from the *Aura* MLS observations. Potential temperature θ is used for the vertical axis. Contour intervals of \overline{MPV} and \overline{MPV}_ϕ are 5 PVU and 15 PVU rad^{-1} , respectively. Green curves show contours of the geopotential height at an interval of 10 km.

(color) climatologies, averaged for $\theta = 3500\text{--}4500$ K, corresponding to $z \sim 75$ km. Negative \overline{MPV}_ϕ regions are observed during nearly the whole year in both hemispheres, suggesting that the necessary condition of BT/BC instability is almost always satisfied in the mesosphere. The $|\overline{MPV}|$ maximum, highlighted by the \overline{MPV} contours of ± 15 PVU ($1 \text{ PVU} = 10^{-6} \text{ K kg}^{-1} \text{ m}^2 \text{ s}^{-1}$) in summer, appears at $\sim 30^\circ\text{N}$ in the middle of May (at $\sim 30^\circ\text{S}$ at the end of November), slowly propagates poleward, and reaches $\sim 60^\circ\text{N}$ at the beginning of October ($\sim 50^\circ\text{S}$ in the middle of March). The winter $|\overline{MPV}|$ maximum is observed at $\sim 50^\circ\text{N}$ ($\sim 50^\circ\text{S}$) for a short period from the middle of December to the middle of January (from the beginning of July to the middle of September).

Figure 7b shows the time–latitude section of the EPFD climatology, averaged for $z = 70\text{--}80$ km by colors instead of \overline{MPV}_ϕ . The contours again show the \overline{MPV} . It is clear that strongly positive EPFD is observed in the strongly negative \overline{MPV}_ϕ region. It is also important that the EPFD is strongly negative equatorward of the \overline{MPV} maximum. This characteristic latitudinal distribution of positive and negative EPFDs corresponds to a large PV flux divergence mitigating the \overline{MPV} maximum (Sato and

Nomoto 2015), as the EPFD is equivalent to the PV flux in the quasigeostrophic (QG) equation system [i.e., $\overline{v'q'} = \rho_0^{-1} \nabla \cdot \mathbf{F}$, where q is PV in the QG system (hereafter referred to as QGPV), and ρ_0 is the basic density].

b. Rossby wave characteristics in the MLT region

In this section, we examine the characteristics of the in situ generated RWs in both the summer and winter mesospheres. First, we show the zonal wavenumber and frequency power spectra of geopotential fluctuations at $\phi = 46.0^\circ\text{S}$ and $z \sim 93$ km (1.8×10^{-3} hPa) in January (i.e., in summer) that were averaged over 11 years from 2005 to 2015, where the EP flux associated with RWs is the largest in the summer MLT region (Fig. 8). Note that migrating tides were removed from the original geopotential data beforehand. A dominant peak is observed at $\tau \sim 1.8$ days and $s = -2$ to -4 (where a minus sign denotes westward-propagating components). This peak is likely due to the so-called QTDWs. Figure 9 shows the same spectra but for $\phi = 54.4^\circ\text{S}$ and $z \sim 71$ km (3.7×10^{-2} hPa) in July (i.e., in winter), averaged over 10 years from 2005 to 2014. Three peaks are seen at $(s, \tau) = (-1, 10)$, $(1, 6\text{--}20)$, and $(1, 3.8)$ days. The third

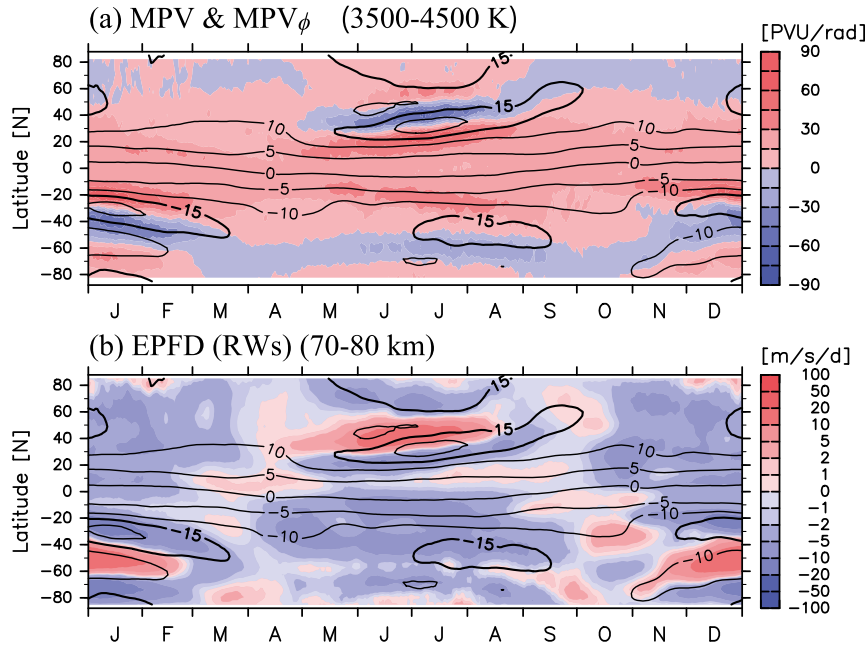


FIG. 7. Time-latitude sections of the climatology of (a) $\overline{\text{MPV}}$ (contours) and $\overline{\text{MPV}}_\phi$ (colors), averaged over $\theta = 3500\text{--}4500\text{ K}$, and (b) $\overline{\text{MPV}}$ (contours) for $\theta = 3500\text{--}4500\text{ K}$ and the EP flux divergence caused by RWs (colors), averaged over $z = 70\text{--}80\text{ km}$. Contour intervals for $\overline{\text{MPV}}$ are 5 PVU. Contours of $\pm 15\text{ PVU}$ are indicated by thick curves to highlight the regions of positive and negative $\overline{\text{MPV}}$ maxima.

peak likely corresponds to the so-called 4-day waves. It is considered that these QTDWs and 4-day waves are radiated to mitigate the BT/BC instability condition of the mean fields.

To confirm this, we analyzed the time change of the RW energy and the energy exchange between the mean flow and RWs using the following wave energy equation (Andrews et al. 1987):

$$\frac{\partial}{\partial t} \left[\frac{1}{2} \rho_0 (\overline{u'^2} + \overline{v'^2} + \overline{\Phi_z'^2}/N^2) \right] + \nabla \cdot (0, \rho_0 \overline{v'\Phi'}, \rho_0 \overline{w'\Phi'}) = -\rho_0 a^{-1} (\overline{u}_\phi + \overline{u} \tan \phi) \overline{v'u'} - \rho_0 \overline{u_z} \overline{w'u'} - \frac{\rho_0 a^{-1} \overline{\theta}_\phi \overline{v'\Phi'}}{\overline{\theta}_z}, \quad (9)$$

where the first and second terms on the left-hand side show the time change of the RW energy and energy flux, respectively, and the right-hand side shows the energy exchange between RWs and the mean field. Figure 10 shows the energy exchange from the mean field to the QTDWs, the standard deviation of temperature fluctuations σ_T associated with the QTDWs, and the latitudinal gradient of the MPV, averaged for a region of $\phi = 20^\circ\text{--}60^\circ\text{S}$ and $z = 65\text{--}80\text{ km}$ ($\theta = 3000\text{--}5000\text{ K}$) in January 2006, when the amplitudes of the QTDWs are largest during the analyzed 12 years. Here, the components with $\tau \sim 1.5\text{--}2.5$ days and $s = -2$ to -4 were analyzed as the QTDWs. The energy transfer from the mean field to the QTDWs increases on 15 January, followed by an increase in σ_T on 18 January. The $\overline{\text{MPV}}_\phi$, which is largely negative on 15 January, gradually

increases and finally becomes positive on 26 January. Such time evolution is consistent with the inference that QTDWs are in situ generated by BT/BC instability to stabilize the background field. While the signals are relatively weak, similar features are also observed in other years (not shown). The time lag among the energy transfer from the mean field, σ_T , and $\overline{\text{MPV}}_\phi$ may be determined by the growth rate, the upward-propagating speed of QTDWs, and the region for the average, although the details are beyond the scope of this paper.

Figure 11 shows the result for the 4-day waves, which are extracted as components with $1 < \tau < 5$ day and $s = 1\text{--}4$, for the region of $\phi = 50^\circ\text{--}70^\circ\text{S}$ and $z = \sim 67\text{--}77\text{ km}$ ($\theta = 3500\text{--}5000\text{ K}$) during July 2007. Similar to the QTDWs, it is seen that the energy transfer from the mean field becomes large after 13 July when σ_T for

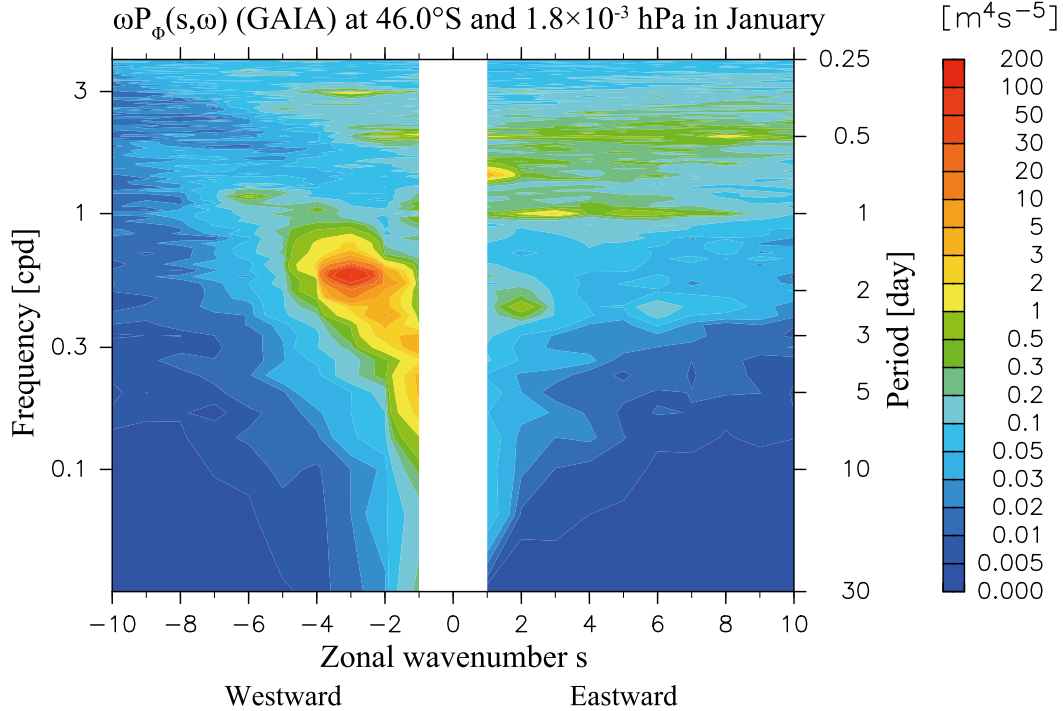


FIG. 8. Climatology of the power spectrum of geopotential in the frequency ω (cycles per day)–zonal wave-number s domain for 46.0°S and $z \sim 93 \text{ km}$ ($1.8 \times 10^{-3} \text{ hPa}$) in January (i.e., SH summer). Negative and positive values of s denote westward- and eastward-propagating components, respectively.

the 4-day waves increases. This process is also consistent with the time evolution of the $\overline{\text{MPV}}_\phi$: the $\overline{\text{MPV}}_\phi$ is largely negative around 13 July but increases after that to mitigate the BT/BC instability condition. This result indicates that the 4-day waves are also likely in situ generated by the BT/BC instability.

c. Physical mechanisms of PV maximum formation in the mesosphere

According to the case study by [Sato and Nomoto \(2015\)](#) using the KANTO model, a gravity wave-resolving GCM, GW forcing is responsible for the PV maximum at middle latitudes of the winter mesosphere: GW forcing causes an upwelling at middle latitudes, increases N^2 , and forms the PV maximum. It is interesting to examine how robust this formation mechanism is and what the difference between the hemispheres is. As already stated, unlike the KANTO model, GAIA uses GW parameterizations to express the forcing by subgrid-scale GWs from the troposphere (i.e., GWF_p). The GWF_p value is largely positive (negative) in the summer (winter) mesosphere (see [Fig. 3](#)).

As mentioned in [section 3b](#), the MPV is proportional to both N^2 and $f + \zeta$. Because usually $|\zeta| \ll |f|$ and $|\delta N^2| \ll |N_0^2|$, where N_0^2 is a typical constant value ($= 3.0 \times 10^{-4} \text{ s}^{-2}$) for the mesosphere and $\delta N^2 = N^2 - N_0^2$, the

MPV is written as a sum of three components in the following:

$$\text{MPV} = A(fN_0^2 + f\delta N^2 + \zeta N_0^2), \quad \text{where} \quad A = \frac{H\theta}{p} \left(\frac{\theta}{\theta_0} \right)^{-9/2}. \quad (10)$$

The second and third terms on the right-hand side are modulations of the MPV by δN^2 (hereafter referred to as $\delta\text{MPV}-N^2$) and by ζ ($\delta\text{MPV}-\zeta$), respectively. [Figure 12](#) shows the meridional cross sections of the climatology of the zonal-mean latitudinal gradients of $\delta\text{MPV}-N^2$ ($\delta\text{MPV}_\phi-N^2$) and $\delta\text{MPV}-\zeta$ ($\delta\text{MPV}_\phi-\zeta$) for January. The zero contours of the $\overline{\text{MPV}}_\phi$ are indicated by thick curves to show the negative $\overline{\text{MPV}}_\phi$ regions. It is clear that the negative $\overline{\text{MPV}}_\phi$ region around 40°S and 4000 K in the summer hemisphere is attributable to both $\delta\text{MPV}_\phi-N^2$ and $\delta\text{MPV}_\phi-\zeta$, while that at high latitudes of the winter hemisphere around 4000 K is mainly due to $\delta\text{MPV}_\phi-N^2$. The latter result for the winter hemisphere is consistent with the case study by [Sato and Nomoto \(2015\)](#).

It is likely that the existence of negative $\overline{\text{MPV}}_\phi$ regions (i.e., the necessary condition for BT/BC instability in both hemispheres) is maintained by the GWF_p . A discussion involving the \overline{w}^* caused by the GWF_p , such as

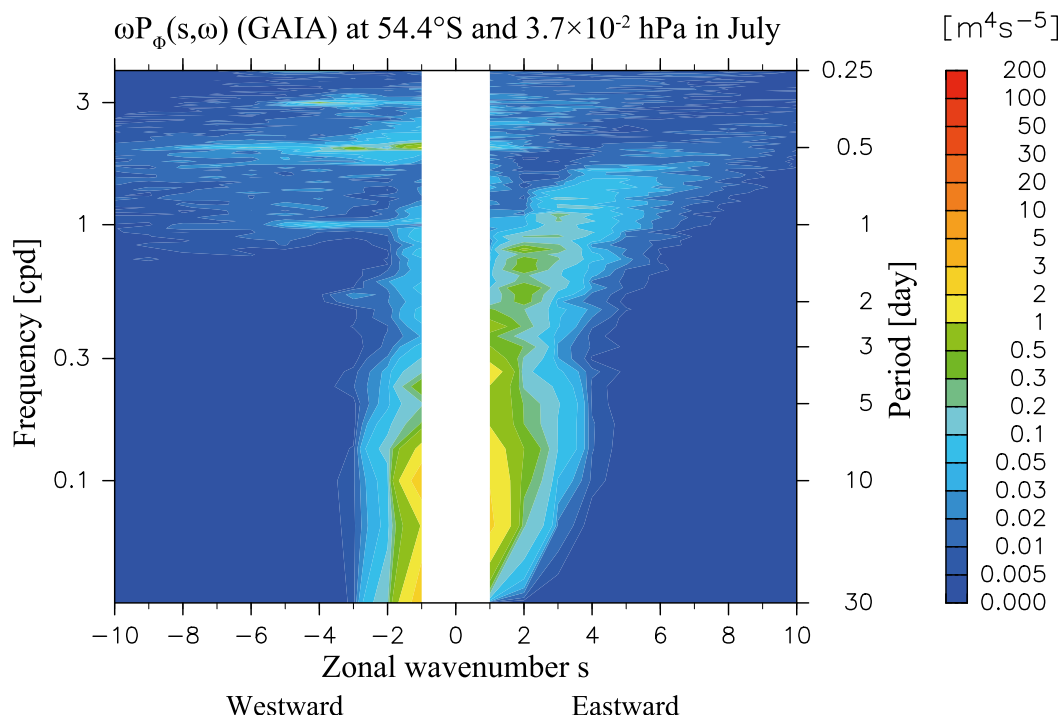


FIG. 9. As in Fig. 8, but for 54.4°S and $z \sim 71$ km (3.7×10^{-2} hPa) in July (i.e., SH winter).

that made by (Sato and Nomoto 2015), is possible. However, this inference is more directly confirmed by using the following QG equation, which relates the meridional QG PV flux with wave forcing:

$$\overline{v'q'} = \frac{1}{\rho_0} \nabla \cdot \mathbf{F} + \overline{X}, \quad (11)$$

where \overline{X} is nongeostrophic wave forcing, such as GW forcing (cf. Andrews et al. 1987). Because the \overline{q} tendency is written using the meridional PV flux,

$$\overline{q}_t = -(\overline{v'q'})_y, \quad (12)$$

the contribution of the parameterized GW forcing to \overline{q}_t is obtained using

$$-\overline{X}_y = -\frac{1}{a \cos \phi} \left| \frac{\partial}{\partial \phi} (\overline{\text{GWF}}_p \cos \phi) \right|_{\theta}. \quad (13)$$

Figure 13 shows the latitude–height sections of the climatology of $-\overline{X}_y$ for January and July. The PV maximum formation mechanism is different for the summer and winter hemispheres. For the summer hemisphere, a negative maximum of $-\overline{X}_y$ is observed in the SH mesospheric region from $(\phi, \theta) = (20^\circ\text{S}, 2500\text{ K})$ to $(40^\circ\text{S}, 7000\text{ K})$ in January, which agrees with the region of the negative $\overline{\text{MPV}}$ maximum (Fig. 4a). Similarly, a positive maximum of $-\overline{X}_y$ is observed in the NH mesosphere

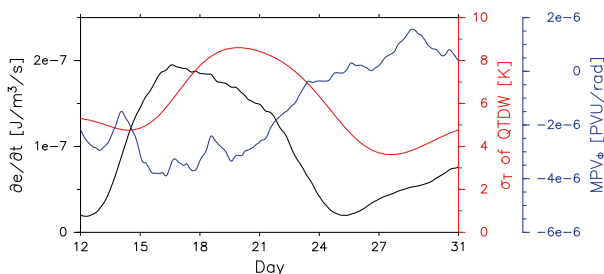


FIG. 10. Time series of the energy exchange from the mean flow to QTDW (black curve), standard deviation of temperature fluctuations associated with QTDWs (red curve), and $\overline{\text{MPV}}_\phi$ (blue curve), which are averaged for the region of $\phi = 20^\circ\text{--}60^\circ\text{S}$ and $z = 65\text{--}80$ km ($\theta = 3000\text{--}5000$ K) for January 2006.

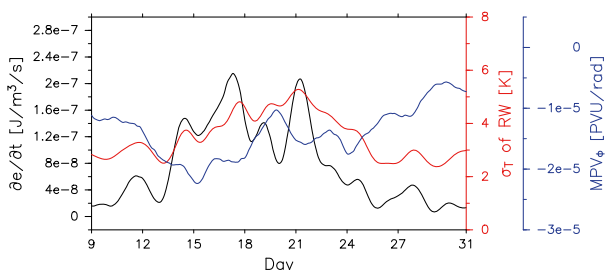


FIG. 11. As in Fig. 10, but for RWs with $s = 1\text{--}4$ and $1 < \tau < 5$ days, including the so-called 4-day waves, averaged for $\phi = 50^\circ\text{--}70^\circ\text{S}$ and $z = \sim 67\text{--}77$ km ($\theta = 3500\text{--}5000$ K) for July 2007.

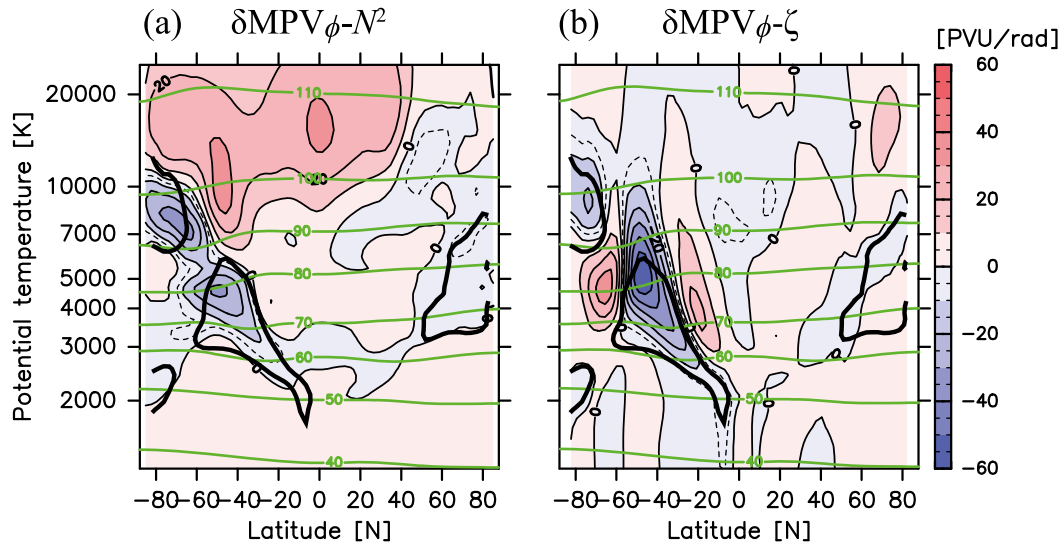


FIG. 12. Meridional cross section of the contribution to $\overline{\text{MPV}}_\phi$ (a) by N^2 departure from the basic state and (b) by relative vorticity ζ for climatology in January. Contour intervals are 10 PVU rad^{-1} , and dashed curves denote -5 PVU rad^{-1} . Zero contours of $\overline{\text{MPV}}_\phi$ in Fig. 4c are also indicated by thick solid curves.

region from $(\phi, \theta) = (20^\circ\text{N}, 2500 \text{ K})$ to $(40^\circ\text{N}, 7000 \text{ K})$ in July, where the positive $\overline{\text{MPV}}$ maximum is observed. In contrast, for the winter hemisphere, largely positive (negative) values are observed in $-\overline{X}_y$ poleward of 50°S

(60°N) and for $\theta = 3000\text{--}7000 \text{ K}$ in the SH (NH) in July (January), which can induce a negative (positive) $\overline{\text{MPV}}$ maximum at $\sim 40^\circ\text{S}$ ($\sim 50^\circ\text{N}$). These results support our inference that the forcing of GWs originating from the

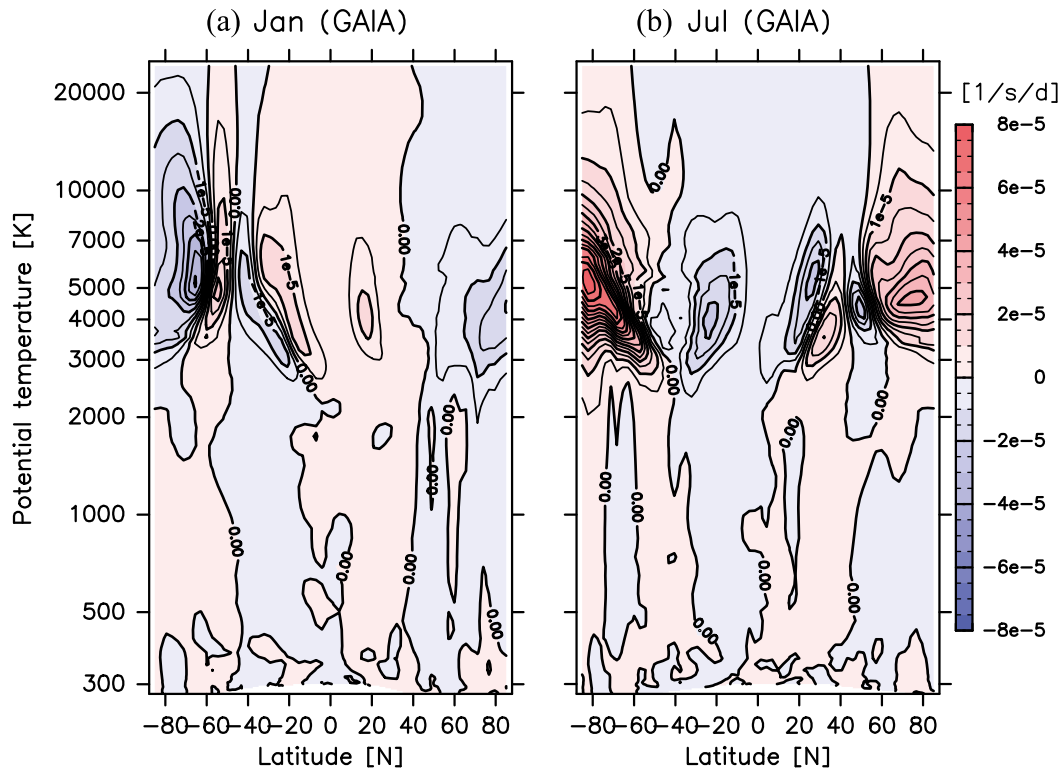


FIG. 13. Meridional cross section of $-\overline{X}_y [= -(\partial/\partial y)\overline{\text{GWF}}_p]$ for climatology in (a) January and (b) July. Contour interval is $5.0 \times 10^{-6} \text{ s}^{-1} \text{ day}^{-1}$.

troposphere causes the BT/BC instability condition in the mesosphere and that the BT/BC instability is the source of the in situ radiation of RWs in the mesosphere.

It is also worth noting that the magnitude of the positive $-\overline{X}_y$ in the SH in July is larger than that of the negative $-\overline{X}_y$ in the NH in January. This hemispheric difference is consistent with the fact that a negative \overline{MPV}_ϕ is more significant for the SH winter than the NH winter. This difference may be reflected by stronger activity of the stratospheric RWs in the NH winter, as stratospheric RWs affect the GW propagation into the mesosphere (Smith 2003; Sato and Nomoto 2015). Note that the difference between the two hemispheres for the summer season is small. This is consistent with the RW activity in summer, which should be equally weak for both hemispheres because the stratospheric mean westward flow prohibits the RW upward propagation.

7. Summary and concluding remarks

This study examined the climatology of the momentum budget in the MLT region using simulation data from a whole-atmosphere model (GAIA) covering ~ 11 years, from August 2004 to June 2015, in terms of the respective wave contributions. Surprisingly, resolved GWs with large amplitudes appeared in the mesosphere and lower thermosphere, regardless of the relatively coarse horizontal resolution of the model whose truncation wavenumber is 42. Thus, four components were analyzed: contributions by 1) RWs, 2) resolved GWs, 3) TWs, and 4) parameterized GW forcing.

It was found that resolved and parameterized GW forcings are comparable and the main contributors to the total wave forcing in the MLT region in all seasons, although the dominant region is slightly higher for resolved GW forcing. TW forcing is dominant at low latitudes of the lower thermosphere, particularly for equinoctial seasons. It is also interesting that large EP flux associated with RWs is observed in both summer and winter MLT regions. The characteristics of the EPFD associated with RWs and resolved GWs suggest that these waves are in situ generated in the mesosphere and significantly contribute to the momentum budget in the MLT region.

Next, the generation mechanisms of RWs in the mesosphere were examined. It was shown that a positive (negative) \overline{MPV} maximum formed at the middle latitudes of the NH (SH) in the mesosphere throughout almost the whole year. Good accordance between negative \overline{MPV}_ϕ and positive RW-induced EPFD regions strongly suggests that the RWs are generated in the mesosphere via the BT/BC instability. Similar features were also seen in the *Aura* MLS observation data.

The RWs in the summer MLT region were mainly $s = 2$ –4 westward-propagating waves having $\tau = \sim 1.8$ days, which is consistent with the QTDWs, while those in the winter MLT region were composed of RWs with various wavenumbers and periods, including the so-called 4-day waves. The time evolutions of the energy exchange rate with the mean flow, wave energy, and \overline{MPV}_ϕ also supported the generation of RWs via the BT/BC instability in the mesosphere. Notably, the \overline{MPV} maximum at middle latitudes was continuously observed despite the RW radiation as a weakening mechanism, suggesting that there is a maintenance mechanism for the BT/BC instability in the mesosphere. Via an analysis using the QG theory, it was concluded that the \overline{MPV} maximum, namely, the necessary condition of the BT/BC instability, is likely maintained by the forcing due to GWs propagating from the troposphere, which was expressed by parameterization schemes in the model.

In summary, it was shown that the momentum budget of the MLT region is attributable not only to RWs and GWs originating from the troposphere but also to contributions made by RWs and GWs that are generated in situ in the mesosphere. The generation of RWs in the mesosphere is largely due to the BT/BC instability caused by the forcing due to GWs from the troposphere. It is also worth noting that the nonlinear dynamics may also be important, particularly in the NH winter, during which strong RW activity was observed. In addition, RW generation in the mesosphere due to filtered GWs and the stratospheric RWs may also be important (Smith 2003). The generation mechanism of GWs in the mesosphere is also an important and interesting issue. The characteristics and generation mechanisms of the resolved GWs in our model will be closely examined in the companion paper (Part II). The importance of the forcing of GWs from the lower atmosphere will again be highlighted.

It is also worth noting here that currently, most of the GW parameterization schemes are applied with some oversimplifications, including the assumption of a steady-state wave field and background flow, instantaneous GW propagation, and one-dimensional vertical propagation. Many authors (Bühler and McIntyre 1999, 2003, 2005; Dosser and Sutherland 2011; Bölöni et al. 2016; Amemiya and Sato 2016) have suggested that important aspects of wave–flow interaction could be neglected due to the above oversimplifications. Thus, there is still room for reducing the model errors due to the oversimplifications of GW parameterizations. However, the significant consistency between *Aura* MLS observations and GAIA model simulation shown in this study indicates that the overall features of the GW momentum transport in the middle atmosphere revealed by this study must be close to the real world.

Acknowledgments. This work was supported by JST CREST JPMJCR1663. The figures were drawn by the GFD-DENNOU library. The numerical simulation in this work was performed using the Hitachi SR16000/M1 and the NICT Science Cloud System, Japan. The *Aura* MLS data were obtained from the Jet Propulsion Laboratory, California Institute of Technology (from ftp://acdsc.gsfc.nasa.gov/data/s4pa/Aura_MLS_Levels/).

REFERENCES

- Amemiya, A., and K. Sato, 2016: A new gravity wave parameterization including three-dimensional propagation. *J. Meteor. Soc. Japan*, **94**, 237–256, <https://doi.org/10.2151/jmsj.2016-013>.
- Andrews, D. G., J. R. Holton, and C. B. Leovy, 1987: *Middle Atmosphere Dynamics*. Academic Press, 489 pp.
- Baldwin, M., and J. Holton, 1988: Climatology of the stratospheric polar vortex and planetary wave breaking. *J. Atmos. Sci.*, **45**, 1123–1142, [https://doi.org/10.1175/1520-0469\(1988\)045<1123:COTSPV>2.0.CO;2](https://doi.org/10.1175/1520-0469(1988)045<1123:COTSPV>2.0.CO;2).
- Baumgaertner, A. J. G., A. J. McDonald, R. E. Hibbins, D. C. Fritts, D. J. Murphy, and R. A. Vincent, 2008: Short-period planetary waves in the Antarctic middle atmosphere. *J. Atmos. Sol.-Terr. Phys.*, **70**, 1336–1350, <https://doi.org/10.1016/j.jastp.2008.04.007>.
- Becker, E., 2012: Dynamical control of the middle atmosphere. *Space Sci. Rev.*, **168**, 283–314, <https://doi.org/10.1007/s11214-011-9841-5>.
- Böläni, G., B. Ribstein, J. Murašchko, C. Sgoff, J. Wei, and U. Achatz, 2016: The interaction between atmospheric gravity waves and large-scale flows: An efficient description beyond the nonacceleration paradigm. *J. Atmos. Sci.*, **73**, 4833–4852, <https://doi.org/10.1175/JAS-D-16-0069.1>.
- Bühler, O., and M. E. McIntyre, 1999: On shear-generated gravity waves that reach the mesosphere. Part II: Wave propagation. *J. Atmos. Sci.*, **56**, 3764–3773, [https://doi.org/10.1175/1520-0469\(1999\)056<3764:OSGGWT>2.0.CO;2](https://doi.org/10.1175/1520-0469(1999)056<3764:OSGGWT>2.0.CO;2).
- , and —, 2003: Remote recoil: A new wave-mean interaction effect. *J. Fluid Mech.*, **492**, 207–230, <https://doi.org/10.1017/S0022112003005639>.
- , and —, 2005: Wave capture and wave-vortex duality. *J. Fluid Mech.*, **534**, 67–95, <https://doi.org/10.1017/S0022112005004374>.
- Butchart, N., 2014: The Brewer–Dobson circulation. *Rev. Geophys.*, **52**, 157–184, <https://doi.org/10.1002/2013RG000448>.
- Charney, J. G., and P. G. Drazin, 1961: Propagation of planetary-scale disturbances from the lower into the upper atmosphere. *J. Geophys. Res.*, **66**, 83–109, <https://doi.org/10.1029/JZ066i001p00083>.
- Cohen, N. Y., E. P. Gerber, and O. Bühler, 2013: Compensation between resolved and unresolved wave driving in the stratosphere: Implications for downward control. *J. Atmos. Sci.*, **70**, 3780–3798, <https://doi.org/10.1175/JAS-D-12-0346.1>.
- Dosser, H. V., and B. Sutherland, 2011: Anelastic internal wave packet evolution and stability. *J. Atmos. Sci.*, **68**, 2844–2859, <https://doi.org/10.1175/JAS-D-11-097.1>.
- Ern, M., P. Preusse, J. C. Gille, C. L. Hepplewhite, M. G. Mlynarczyk, J. M. Russell III, and M. Riese, 2011: Implications for atmospheric dynamics derived from global observations of gravity wave momentum flux in stratosphere and mesosphere. *J. Geophys. Res.*, **116**, D19107, <https://doi.org/10.1029/2011JD015821>.
- , —, S. Kalisch, M. Kaufmann, and M. Riese, 2013: Role of gravity waves in the forcing of quasi two-day waves in the mesosphere: An observational study. *J. Geophys. Res. Atmos.*, **118**, 3467–3485, <https://doi.org/10.1029/2012JD018208>.
- Fomichev, V. I., W. E. Ward, S. R. Beagley, C. McLandress, J. C. McConnell, N. A. McFarlane, and T. G. Shepherd, 2002: Extended Canadian Middle Atmosphere Model: Zonal-mean climatology and physical parameterizations. *J. Geophys. Res.*, **107**, <https://doi.org/10.1029/2001JD000479>.
- Garcia, R. R., R. Lieberman, J. M. Russell, and M. G. Mlynarczyk, 2005: Large-scale waves in the mesosphere and lower thermosphere observed by SABER. *J. Atmos. Sci.*, **62**, 4384–4399, <https://doi.org/10.1175/JAS3612.1>.
- , D. R. Marsh, D. E. Kinnison, B. A. Boville, and F. Sassi, 2007: Simulation of secular trends in the middle atmosphere, 1950–2003. *J. Geophys. Res.*, **112**, D09301, <https://doi.org/10.1029/2006JD007485>.
- Geller, M. A., and Coauthors, 2013: A comparison between gravity wave momentum fluxes in observations and climate models. *J. Climate*, **26**, 6383–6405, <https://doi.org/10.1175/JCLI-D-12-00545.1>.
- Greer, K., J. P. Thayer, and V. L. Harvey, 2013: A climatology of polar winter stratospheric warmings and associated planetary wave breaking. *J. Geophys. Res. Atmos.*, **118**, 4168–4180, <https://doi.org/10.1002/jgrd.50289>.
- Gu, S.-Y., H.-L. Liu, N. M. Pedatella, X. Dou, T. Li, and T. Chen, 2016: The quasi 2 day wave activities during 2007 austral summer period as revealed by Whole Atmosphere Community Climate Model. *J. Geophys. Res. Space Phys.*, **121**, 2743–2754, <https://doi.org/10.1002/2015JA022225>.
- Holton, J. R., 1983: The influence of gravity wave breaking on the general circulation of the middle atmosphere. *J. Atmos. Sci.*, **40**, 2497–2507, [https://doi.org/10.1175/1520-0469\(1983\)040<2497:TIOGWB>2.0.CO;2](https://doi.org/10.1175/1520-0469(1983)040<2497:TIOGWB>2.0.CO;2).
- , 1984: The generation of mesospheric planetary waves by zonally asymmetric gravity wave breaking. *J. Atmos. Sci.*, **41**, 3427–3430, [https://doi.org/10.1175/1520-0469\(1984\)041<3427:TGOMPW>2.0.CO;2](https://doi.org/10.1175/1520-0469(1984)041<3427:TGOMPW>2.0.CO;2).
- Iida, C., T. Hirooka, and N. Eguchi, 2014: Circulation changes in the stratosphere and mesosphere during the stratospheric sudden warming event in January 2009. *J. Geophys. Res. Atmos.*, **119**, 7104–7115, <https://doi.org/10.1002/2013JD021252>.
- Jin, H., and Coauthors, 2011: Vertical connection from the tropospheric activities to the ionospheric longitudinal structure simulated by a new Earth’s whole atmosphere-ionosphere coupled model. *J. Geophys. Res.*, **116**, A01316, <https://doi.org/10.1029/2010JA015925>.
- Lait, L. R., 1994: An alternative form for potential vorticity. *J. Atmos. Sci.*, **51**, 1754–1759, [https://doi.org/10.1175/1520-0469\(1994\)051<1754:AAFFPV>2.0.CO;2](https://doi.org/10.1175/1520-0469(1994)051<1754:AAFFPV>2.0.CO;2).
- Lawrence, B. N., and W. J. Randel, 1996: Variability in the mesosphere observed by the Nimbus 6 pressure modulator radiometer. *J. Geophys. Res.*, **101**, 23 475–23 489, <https://doi.org/10.1029/96JD01652>.
- Lieberman, R. S., 1999: Eliassen–Palm fluxes of the 2-day wave. *J. Atmos. Sci.*, **56**, 2846–2861, [https://doi.org/10.1175/1520-0469\(1999\)056<2846:EPFOTD>2.0.CO;2](https://doi.org/10.1175/1520-0469(1999)056<2846:EPFOTD>2.0.CO;2); Corrigendum, **59**, 2625–2627, [https://doi.org/10.1175/1520-0469\(2002\)059<2625:C>2.0.CO;2](https://doi.org/10.1175/1520-0469(2002)059<2625:C>2.0.CO;2).
- , and P. B. Hays, 1994: An estimate of the momentum deposition in the lower thermosphere by the observed diurnal tide. *J. Atmos. Sci.*, **51**, 3094–3105, [https://doi.org/10.1175/1520-0469\(1994\)051<3094:AEOTMD>2.0.CO;2](https://doi.org/10.1175/1520-0469(1994)051<3094:AEOTMD>2.0.CO;2).

- Limpasuvan, V., and D. L. Wu, 2003: Two-day wave observations of UARS Microwave Limb Sounder mesospheric water vapor and temperature. *J. Geophys. Res.*, **108**, 1–12, <https://doi.org/10.1029/2002JD002903>.
- Lindzen, R. S., 1981: Turbulence and stress owing to gravity wave and tidal breakdown. *J. Geophys. Res.*, **86**, 9707–9714, <https://doi.org/10.1029/JC086iC10p09707>.
- Manney, G. L., and W. J. Randel, 1993: Instability at the winter stratopause: A mechanism for the 4-day wave. *J. Atmos. Sci.*, **50**, 3928–3938, [https://doi.org/10.1175/1520-0469\(1993\)050<3928:IATWSA>2.0.CO;2](https://doi.org/10.1175/1520-0469(1993)050<3928:IATWSA>2.0.CO;2).
- Matsuno, T., 1982: A quasi one-dimensional model of the middle atmosphere circulation interacting with internal gravity waves. *J. Meteor. Soc. Japan*, **60**, 215–226, https://doi.org/10.2151/jmsj1965.60.1_215.
- McFarlane, N. A., 1987: The effect of orographically excited gravity wave drag on the general circulation of the lower stratosphere and troposphere. *J. Atmos. Sci.*, **44**, 1775–1800, [https://doi.org/10.1175/1520-0469\(1987\)044<1775:TEOOEG>2.0.CO;2](https://doi.org/10.1175/1520-0469(1987)044<1775:TEOOEG>2.0.CO;2).
- McLandress, C., W. E. Ward, V. I. Fomichev, K. Semeniuk, S. R. Beagley, N. A. McFarlane, and T. G. Shepherd, 2006: Large-scale dynamics of the mesosphere and lower thermosphere: An analysis using the extended Canadian Middle Atmosphere Model. *J. Geophys. Res.*, **111**, D17111, <https://doi.org/10.1029/2005JD006776>.
- Medvedeva, I., A. Semenov, V. Perminov, A. Beletsky, and A. Tatarnikov, 2014: Comparison of ground-based OH temperature data measured at Irkutsk (52°N, 103°E) and Zvenigorod (56°N, 37°E) stations with Aura MLS v3.3. *Acta Geophys.*, **62**, 340–349, <https://doi.org/10.2478/s11600-013-0161-x>.
- Miyahara, S., Y. Miyoshi, and K. Yamashita, 1999: Variations of migrating and non-migrating tides simulated by the Middle Atmosphere Circulation Model at Kyushu University. *Adv. Space Res.*, **24**, 1549–1558, [https://doi.org/10.1016/S0273-1177\(99\)00879-0](https://doi.org/10.1016/S0273-1177(99)00879-0).
- Miyoshi, Y., and H. Fujiwara, 2003: Day-to-day variations of migrating diurnal tide simulated by a GCM from the ground surface to the exobase. *Geophys. Res. Lett.*, **30**, 1789, <https://doi.org/10.1029/2003GL017695>.
- , —, H. Jin, and H. Shinagawa, 2014: A global view of gravity waves in the thermosphere simulated by a general circulation model. *J. Geophys. Res. Space Phys.*, **119**, 5807–5820, <https://doi.org/10.1002/2014JA019848>.
- Mukhtarov, P., D. Pancheva, and B. Andonov, 2009: Global structure and seasonal and interannual variability of the migrating diurnal tide seen in the SABER/TIMED temperatures between 20 and 120 km. *J. Geophys. Res.*, **114**, A02309, <https://doi.org/10.1029/2008JA013759>.
- Murphy, D. J., W. J. R. French, and R. A. Vincent, 2007: Long-period planetary waves in the mesosphere and lower thermosphere above Davis, Antarctica. *J. Atmos. Sol.-Terr. Phys.*, **69**, 2118–2138, <https://doi.org/10.1016/j.jastp.2007.06.008>.
- Norton, W. A., and J. Thuburn, 1999: Sensitivity of mesospheric mean flow, planetary waves, and tides to strength of gravity wave drag. *J. Geophys. Res.*, **104**, 30 897–30 911, <https://doi.org/10.1029/1999JD900961>.
- Onogi, K., and Coauthors, 2007: The JRA-25 Reanalysis. *J. Meteor. Soc. Japan*, **85**, 369–432, <https://doi.org/10.2151/jmsj.85.369>.
- Pancheva, D., P. Mukhtarov, D. E. Siskind, and A. K. Smith, 2016: Global distribution and variability of quasi 2 day waves based on the NOGAPS-ALPHA reanalysis model. *J. Geophys. Res. Space Phys.*, **121**, 11 422–11 449, <https://doi.org/10.1002/2016JA023381>.
- Plumb, R., 1983: Baroclinic instability of the summer mesosphere: A mechanism for the quasi-two-day wave? *J. Atmos. Sci.*, **40**, 262–270, [https://doi.org/10.1175/1520-0469\(1983\)040<0262:BIOTSM>2.0.CO;2](https://doi.org/10.1175/1520-0469(1983)040<0262:BIOTSM>2.0.CO;2).
- , 2002: Stratospheric transport. *J. Meteor. Soc. Japan*, **80**, 793–809, <https://doi.org/10.2151/jmsj.80.793>.
- Prata, A. J., 1984: The 4-day wave. *J. Atmos. Sci.*, **41**, 150–155, [https://doi.org/10.1175/1520-0469\(1984\)041<0150:TDW>2.0.CO;2](https://doi.org/10.1175/1520-0469(1984)041<0150:TDW>2.0.CO;2).
- Randel, W. J., 1987: The evaluation of winds from geopotential height data in the stratosphere. *J. Atmos. Sci.*, **44**, 3097–3120, [https://doi.org/10.1175/1520-0469\(1987\)044<3097:TEOWFG>2.0.CO;2](https://doi.org/10.1175/1520-0469(1987)044<3097:TEOWFG>2.0.CO;2).
- Sakazaki, T., K. Sato, Y. Kawatani, and S. Watanabe, 2015: Three-dimensional structures of tropical nonmigrating tides in a high-vertical-resolution general circulation model. *J. Geophys. Res. Atmos.*, **120**, 1759–1775, <https://doi.org/10.1002/2014JD022464>.
- Salby, M. L., and R. G. Roper, 1980: Long-period oscillations in the meteor region. *J. Atmos. Sci.*, **37**, 237–244, [https://doi.org/10.1175/1520-0469\(1980\)037<0237:LPOITM>2.0.CO;2](https://doi.org/10.1175/1520-0469(1980)037<0237:LPOITM>2.0.CO;2).
- , and P. F. Callaghan, 2001: Seasonal amplification of the 2-day wave: Relationship between normal mode and instability. *J. Atmos. Sci.*, **58**, 1858–1869, [https://doi.org/10.1175/1520-0469\(2001\)058<1858:SAOTDW>2.0.CO;2](https://doi.org/10.1175/1520-0469(2001)058<1858:SAOTDW>2.0.CO;2).
- Sato, K., and M. Nomoto, 2015: Gravity wave-induced anomalous potential vorticity gradient generating planetary waves in the winter mesosphere. *J. Atmos. Sci.*, **72**, 3609–3624, <https://doi.org/10.1175/JAS-D-15-0046.1>.
- , and Coauthors, 2014: Program of the Antarctic Syowa MST/IS radar (PANSY). *J. Atmos. Sol.-Terr. Phys.*, **118**, 2–15, <https://doi.org/10.1016/j.jastp.2013.08.022>.
- , M. Kohma, M. Tsutsumi, and T. Sato, 2017: Frequency spectra and vertical profiles of wind fluctuations in the summer Antarctic mesosphere revealed by MST radar observations. *J. Geophys. Res. Oceans*, **122**, 775–787, <https://doi.org/10.1002/2016JC012197>.
- Schwartz, M. J., and Coauthors, 2008: Validation of the Aura Microwave Limb Sounder temperature and geopotential height measurements. *J. Geophys. Res.*, **113**, D15S11, <https://doi.org/10.1029/2007JD008783>.
- Smith, A. K., 2003: The origin of stationary planetary waves in the upper mesosphere. *J. Atmos. Sci.*, **60**, 3033–3041, [https://doi.org/10.1175/1520-0469\(2003\)060<3033:TOOSPW>2.0.CO;2](https://doi.org/10.1175/1520-0469(2003)060<3033:TOOSPW>2.0.CO;2).
- Venne, D. E., and J. L. Stanford, 1979: Observation of a 4-day temperature wave in the polar winter stratosphere. *J. Atmos. Sci.*, **36**, 2016–2019, [https://doi.org/10.1175/1520-0469\(1979\)036<2016:OOATWI>2.0.CO;2](https://doi.org/10.1175/1520-0469(1979)036<2016:OOATWI>2.0.CO;2).
- Watanabe, S., Y. Kawatani, Y. Tomikawa, K. Miyazaki, M. Takahashi, and K. Sato, 2008: General aspects of a T213L256 middle atmosphere general circulation model. *J. Geophys. Res.*, **113**, D12110, <https://doi.org/10.1029/2008JD010026>.
- , Y. Tomikawa, K. Sato, Y. Kawatani, K. Miyazaki, and M. Takahashi, 2009: Simulation of the eastward 4-day wave in the Antarctic winter mesosphere using a gravity wave resolving general circulation model. *J. Geophys. Res.*, **114**, D16111, <https://doi.org/10.1029/2008JD011636>.
- Waters, J. W., and Coauthors, 2006: The Earth Observing System Microwave Limb Sounder (EOS MLS) on the Aura satellite. *IEEE Trans. Geosci. Remote Sens.*, **44**, 1075–1092, <https://doi.org/10.1109/TGRS.2006.873771>.
- Wu, D. H., S. Miyahara, and Y. Miyoshi, 1989: A nonlinear simulation of the thermal diurnal tide. *J. Atmos. Terr. Phys.*, **51**, 1017–1030, [https://doi.org/10.1016/0021-9169\(89\)90017-2](https://doi.org/10.1016/0021-9169(89)90017-2).
- Wu, D. L., E. F. Fishbein, W. G. Read, and J. W. Waters, 1996: Excitation and evolution of the quasi-2-day wave observed in

- UARS/MLS temperature measurements. *J. Atmos. Sci.*, **53**, 728–738, [https://doi.org/10.1175/1520-0469\(1996\)053<0728:EAEOTQ>2.0.CO;2](https://doi.org/10.1175/1520-0469(1996)053<0728:EAEOTQ>2.0.CO;2).
- Wu, Q., and Coauthors, 2006: TIMED Doppler interferometer (TIDI) observations of migrating diurnal and semidiurnal tides. *J. Atmos. Sol.-Terr. Phys.*, **68**, 408–417, <https://doi.org/10.1016/j.jastp.2005.02.031>.
- Yasui, R., K. Sato, and Y. Miyoshi, 2018: The momentum budget in the stratosphere, mesosphere, and lower thermosphere. Part II: The in situ generation of gravity waves. *J. Atmos. Sci.*, **75**, 3635–3651, <https://doi.org/10.1175/JAS-D-17-0337.1>.
- Yue, J., W. Wang, A. D. Richmond, and H. L. Liu, 2012: Quasi-two-day wave coupling of the mesosphere and lower thermosphere-ionosphere in the TIME-GCM: Two-day oscillations in the ionosphere. *J. Geophys. Res.*, **117**, A07305, <https://doi.org/10.1029/2012JA017815>.
- Zhu, X., J.-H. Yee, E. R. Talaat, M. Mlynchak, J. M. Russell, and J. M. Russell III, 2008: Diagnostic analysis of tidal winds and the Eliassen–Palm flux divergence in the mesosphere and lower thermosphere from TIMED/SABER temperatures. *J. Atmos. Sci.*, **65**, 3840–3859, <https://doi.org/10.1175/2008JAS2801.1>.